National Library of Canada
Bibliothèque nationale du Canada

Canadian Theses Service
Service des thèses canadiennes

Ottawa, Canada
K1A 0N4

NOTICE

The quality of this microform is heavily dependent upon the quality of the original thesis submitted for microfilming. Every effort has been made to ensure the highest quality of reproduction possible.

If pages are missing, contact the university which granted the degree.

Some pages may have indistinct print especially if the original pages were typed with a poor typewriter ribbon or if the university sent us an inferior photocopy.

Reproduction in full or in part of this microform is governed by the Canadian Copyright Act, R.S.C. 1970, c. C-30, and subsequent amendments.

AVIS

La qualité de cette microforme dépend grandement de la qualité de la thèse soumise au microfilmage. Nous avons tout fait pour assurer une qualité supérieure de reproduction.

S'il manque des pages, veuillez communiquer avec l'université qui a conféré le grade.

La qualité d'impression de certaines pages peut laisser à désirer, surtout si les pages originales ont été dactylographiées à l'aide d'un ruban usé ou si l'université nous a fait parvenir une photocopie de qualité inférieure.

La reproduction, même partielle, de cette microforme est soumise à la Loi canadienne sur le droit d'auteur, SRC 1970, c. C-30, et ses amendements subséquents.

NL-339 (r. 88/04) c

Canada

UNIVERSITY OF ALBERTA

PROPELLER ANALYSIS AND DESIGN

BY

BRAD D. MURRAY

A thesis submitted to the Faculty of Graduate Studies and Research in partial fulfillment of the requirements for the degree of MASTER OF SCIENCE.

DEPARTMENT OF MECHANICAL ENGINEERING

EDMONTON, ALBERTA

SPRING 1992

National Library of Canada
Bibliothèque nationale du Canada

Canadian Theses Service
Service des thèses canadiennes

Ottawa, Canada
K1A 0N4

The author has granted an irrevocable non-exclusive licence allowing the National Library of Canada to reproduce, loan, distribute or sell copies of his/her thesis by any means and in any form or format, making this thesis available to interested persons.

L'auteur a accordé une licence irrévocable et non exclusive permettant à la Bibliothèque nationale du Canada de reproduire, prêter, distribuer ou vendre des copies de sa thèse de quelque manière et sous quelque forme que ce soit pour mettre des exemplaires de cette thèse à la disposition des personnes intéressées.

The author retains ownership of the copyright in his/her thesis. Neither the thesis nor substantial extracts from it may be printed or otherwise reproduced without his/her permission.

L'auteur conserve la propriété du droit d'auteur qui protège sa thèse. Ni la thèse ni des extraits substantiels de celle-ci ne doivent être imprimés ou autrement reproduits sans son autorisation.

ISBN 0-315-73148-6

Canada

UNIVERSITY OF ALBERTA

RELEASE FORM

NAME OF AUTHOR: BRAD D. MURRAY

TITLE OF THESIS: PROPELLER ANALYSIS AND DESIGN

DEGREE: MASTER OF SCIENCE

YEAR THIS DEGREE GRANTED: SPRING 1992

Permission is hereby granted to the University of Alberta Library to reproduce single copies of this thesis and to lend or sell such copies for private, scholarly or scientific research purposes only.

The author reserves all other publication and other rights in association with the copyright in the thesis, and except as hereinbefore provided neither the thesis nor any substantial portion thereof may be printed or otherwise reproduced in any material form whatever without the author's prior written permission.

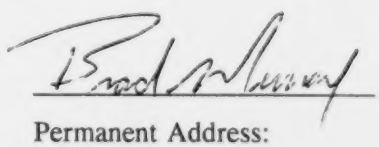

Permanent Address:
14204 - 78 Street
Edmonton, Alberta
T5C 1H5

DATED 31 March 1992

UNIVERSITY OF ALBERTA

FACULTY OF GRADUATE STUDIES AND RESEARCH

The undersigned certify that they have read, and recommend to the Faculty of Graduate Studies and Research for acceptance, a thesis entitled PROPELLER ANALYSIS AND DESIGN submitted by BRAD D. MURRAY in partial fulfillment of the requirements for the degree of MASTER OF SCIENCE.

Dr. D. J. Marsden
Supervisor

Dr. L. W. Sigurdson

Dr. S. M. Kresta

DATED 30 March 1992

I dedicate this work to my wife Alison

Whose unconditional love is a continuous inspiration

ABSTRACT

Recently much emphasis has been placed on the development of precise numerical models for the propeller vortex wake, which ultimately should increase the accuracy and reliability of optimum design and analysis methods. However, propeller designers working within the light aircraft industry often have limited computer resources and therefore require a less complex and less time intensive approach. Utilizing the now classical propeller theory, efficient analysis and design routines appropriate for lightly loaded propellers have been developed.

The analysis routine is based upon blade element and momentum theory and is shown to agree well with experimental results. The iterative solution does demonstrate poor convergence near the tips of blunt ended blades but this difficulty has been overcome by introducing a control point just off the blade tip.

An optimum propeller is designed such that specific performance requirements are met and the induced losses are minimized. A helicoidal vortex wake of constant displacement velocity corresponds to minimal induced losses and has therefore been used as the basis for determining the optimum blade shape. The design routine is verified by the analysis routine in that the performance characteristics obtained from analysis of the optimum blade shape match the performance for which the propeller was designed.

These routines are executed very efficiently on personal computers which has facilitated the actual design and analysis of a lightly loaded propeller. An optimum propeller was designed for a light aircraft that was to operate efficiently at speeds of 50 to 200 mph with an 80 HP engine.

ACKNOWLEDGEMENT

I would like to express my appreciation and thanks to Dr. D. Marsden for his supervision, assistance, and patience throughout this project. I would also thank Mr. P. Hassell and Mr. P. Methven of Dowty Aerospace for their assistance during the early stages of this project.

TABLE OF CONTENTS

Chapter 1, Introduction 1

1.1 History of the Propeller 1

1.2 Development of Propeller Theory 2

1.3 Practical Approach to Analysis and Design 3

Chapter 2, Propeller Theory 4

2.1 Froude's Actuator Disc / Momentum Theory 4

2.1.1 Inflow Velocity 4

2.1.2 Ideal Efficiency (Froude) 10

2.1.3 Extension of Actuator Disc Theory 10

2.2 Blade Element Theory 11

2.3 Condition for Minimum Induced Losses (Betz) 14

2.3.1 Optimum Vortex Wake 17

2.3.2 Optimum Blade Circulation 18

2.4 Prandtl's Momentum Losses 19

2.5 Flow Field Around an Axi-Symmetric Body 27

Chapter 3, Analysis 30

3.1 Derivation of Governing Equations 30

3.1.1 Nacelle Interference 35

3.2 Numerical Solution 36

3.2.1 Convergence Criterion 40

3.2.2 Fixed Pitch 42

3.2.2.1 Approximate Aerodynamic Stall Characteristics 43

3.2.3 Variable Pitch 44

3.3 Verification 45

Chapter 4, Design 56
4.1 Derivation of Governing Equations 56
4.1.1 Constraints 64
4.2 Numerical Solution 68
4.2.1 Convergence Criterion 71
4.2.2 Blade Tip Modification 73
4.3 Verification 74
4.4 Optimization 76

Chapter 5, Light Aircraft Application 78
5.1 Design Requirements 78
5.2 Optimum Design 82
5.2.1 Blade Geometry 87
5.2.2 Performance Characteristics 89

Chapter 6, Conclusions 95
6.1 Validation of the Analysis and Design Routines 95
6.2 Design and Analysis of a Light Aircraft Propeller 96
6.3 Further Research 97

Appendix 101
A.1 Optimum Circulation Distributions 101

LIST OF TABLES

TABLE 1 Optimum Circulation Distribution for 2 & 4 Bladed Propellers at an Advance Ratio of .628 25

TABLE 2 Optimum Circulation Distribution for a 2 Bladed Propeller 25

TABLE 3 Propeller Geometry 45

TABLE 4 Measured vs. Calculated RPM for Test Propeller 53

TABLE 5 Measured vs. Calculated RPM for 3 Modified Prandtl Distributions . 55

TABLE 6 Design Verification Against Analytical Parameters 75

TABLE 6 Advance Ratio and Vortex Sheet Spacing 90

TABLE A1 Optimum Circulation Functions (2 blades, J=1.57) 101

TABLE A2 Optimum Circulation Functions (2 blades, J=1.05) 102

TABLE A3 Optimum Circulation Functions (2 bladed, J=0.785) 103

TABLE A4 Optimum Circulation Functions (2 blades, J=0.628) 104

TABLE A5 Optimum Circulation Functions (2 blades, J=0.392) 105

TABLE A6 Optimum Circulation Functions (4 blades, J=0.628) 106

LIST OF FIGURES

FIGURE 1 Momentum - Bernoulli / Froude 5

FIGURE 2 Axial Inflow Velocities - Momentum 6

FIGURE 3 Rotation Inflow Velocities - Momentum 8

FIGURE 4 Blade Element Theory 11

FIGURE 5 Modified Blade Element Theory 13

FIGURE 6 Idealized Blade Element - No Losses 14

FIGURE 7 Optimum Wake - Frictional Considerations 16

FIGURE 8 Inflow Velocities Induced by the Vortex Wake 16

FIGURE 9 Vortex Filament Trace 17

FIGURE 10 Induced Velocity Distribution (Prandtl) 19

FIGURE 11 Velocity Distribution, Semi-Infinite Plates 20

FIGURE 12 Goldstein's Exact and Prandtl's Approximate Circulation Functions for 2 and 4 Bladed Propellers 24

FIGURE 13 Goldstein's Exact and Prandtl's Approximate Circulation Functions for a 2 Bladed Propeller 26

FIGURE 14 Nacelle Interference 27

FIGURE 15 Momentum - Blade Element Considerations 30

FIGURE 16 Momentum Loss Factor w.r.t. Vortex Sheets 31

FIGURE 17 Wake and Inflow Velocities 32

FIGURE 18 Blade Element Theory 33

FIGURE 19 Airfoil Stall Characteristics 43

FIGURE 20 Blade Airfoil Coordinates for Test Propeller 46

FIGURE 21 Lift and Drag Curves for Test Propeller 47

FIGURE 22 Rotax 532 Performance Curve 48

FIGURE 23 Efficiency vs. Forward Velocity 49

FIGURE 24 Blade RPM vs. Forward Velocity 50

FIGURE 25 Tip Mach Number vs. Forward Velocity 50

FIGURE 26 Engine Power vs. Forward Velocity 51

FIGURE 27 Coefficient of Power vs. Forward Velocity 51

FIGURE 28 Propeller Thrust vs. Forward Velocity 52

FIGURE 29 Coefficient of Thrust vs. Forward Velocity 52

FIGURE 30 Prandtl's Distribution, Modified 54

FIGURE 31 Blade Element Theory 58

FIGURE 32 Vector Diagram of Design Induced Velocities 62

FIGURE 33 Effect of Friction on Optimum Design Condition 63

FIGURE 34 Subaru Engine Performance Curve 79

FIGURE 35 Blade Airfoil Characteristics (Eppler 850 Series) 80

FIGURE 36 Lift and Drag Characteristics (Eppler 850 Series) 81

FIGURE 37 Performance Curves for Design Iteration #1 83

FIGURE 38 Performance Curves for Design Iteration #2 84

FIGURE 39 Performance Curves for Design Iteration #3 85

FIGURE 40 Blade Angle as Designed 87

FIGURE 41 Blade Chord as Designed 88

FIGURE 42 Propeller Efficiency vs. Advance Ratio 91

FIGURE 43 Propeller Efficiency vs. Forward Velocity 91

FIGURE 44 Blade RPM vs. Forward Velocity 92

FIGURE 45 Blade Tip Mach Number vs. Forward Velocity 92

FIGURE 46 Engine Power vs. Forward Velocity 93

FIGURE 47 Coefficient of Power vs. Forward Velocity 93

FIGURE 48 Propeller Thrust vs. Forward Velocity 94

FIGURE 49 Coefficient of Thrust vs. Forward Velocity 94

NOMENCLATURE

a	Axial inflow velocity factor
a'	Rotational inflow velocity factor
A	Propeller disc area
A_s	Source strength
B	Number of blades
C	Chord
C_L	Coefficient of lift
C_D	Coefficient of drag
C_T	Coefficient of thrust (Analysis)
C_P	Coefficient of power (Analysis)
d	Trailing vortex sheet spacing
d_n	Nacelle diameter
D_p	Propeller diameter
D	Drag
D'	Drag per unit radius
F,f	Prandtl's momentum loss factors
G	Optimum circulation function
H	Angular momentum
J	Advance Ratio ($=V/nD_p$)
L	Lift

L'	Lift per unit radius
$\dot{m}$	Mass flow rate
n	Propeller angular velocity (revs/sec)
P_c	Power coefficient (Design)
P	Pressure
q	Volume flow rate
Q	Torque
r	Radius
r_0	Hub radius
R	Blade tip radius
SOS	Speed of sound
T	Thrust
T_c	Thrust coefficient (Design)
u	Axial freestream velocity ratio due to nacelle interference
U	Velocity relative to control volume
V	Uniform free-stream velocity
v'	Vortex wake displacement velocity
v_1	Axial inflow velocity
v_2	Incremental axial velocity in the far wake
ω_1	Rotational inflow velocity
ω_2	Incremental rotational velocity in the far wake
w	Slipstream velocity

W	Relative velocity (V_{rel})
W_1	Relaxation factor for axial inflow factors
W_2	Relaxation factor for rotational inflow factors
W_3	Relaxation factor for Mach Number
W_4	Relaxation factor for displacement velocity
zll	Zero lift line

GREEK SYMBOLS

α	Angle of attact
β	Blade twist angle
Γ	Circulation
$\overline{\Gamma}$	Vortex sheet density
Δ	Increment
ϵ	Ratio of blade element drag to lift
ζ	Displacement velocity factor (=v'/V)
η	Efficiency
κ_c	Ratio used in derivation of optimum wake
λ	Speed Ratio (=V/ΩR)
ξ	Dimensionless radius (=r/R)
ρ	Density
σ	Solidity ratio

ϕ	Angle of relative velocity vector, W
χ	Inverse of Speed Ratio ($=\Omega R/V$)
Ω	Propeller angular velocity (rads/sec)

SUBSCRIPTS

a	Axial
e	Element
n	Normal
r	Blade radius
R	Blade tip radius
s	Slipstream
t	Tangential
T	Blade tip
x	component in x (axial) direction

Chapter 1

Introduction

1.0 INTRODUCTION

1.1 HISTORY OF THE PROPELLER

The propeller, as a means of transmitting energy to a medium such as air or water has been implemented successfully since ancient times. The Chinese constructed flying tops as early as 400 B.C., the Archimedes screw was developed by 200 B.C., and circa 1500 A.D. Leonardo DaVinci first proposed the Archimede's screw for aerial propulsion [1]. The full potential of the propeller however, was not realized until the turn of the 20th century, when the ship and aircraft industry began implementing the propeller into propulsion systems.

Aircraft propellers developed during the early 1900's were predominately manufactured out of wood and commonly consisted of two blades. Pitch angle and chord varied along the blade radius but for quite some time these blade geometries were arrived at somewhat arbitrarily. In spite of the fact that the early pioneers of the propeller lacked appropriate analytical techniques and had to rely heavily on intuition and experimentation, propellers were successfully designed and manufactured. One of the most famous cases is the dual counter-rotating propeller configuration used by the Wright brothers on their first successful flight in 1904 [2].

During the 1930's and throughout the second world war propeller theory advanced very quickly, as did most other engineering fields. A fuller understanding of the principles governing propeller aerodynamics led to more efficient propellers, and the introduction of metal as the primary construction material led to stronger and more reliable propellers. The metal propeller was somewhat heavier than its wood counterpart, but the high strength and improved reliability was thought to be well worth the weight penalty. Also, inspired by the demand for faster fighter aircraft during World War II, the variable pitched propeller was developed [3]. In contrast to the fixed pitch the variable pitch propeller could operate efficiently over a large speed range.

The post war era saw very few advances in propeller technology as jet propulsion was felt to be the way of the future. However due to ever increasing fuel costs a more efficient propulsion system than the jet has become desirable and is quickly becoming necessary. The propeller has a relatively high efficiency due to the fact that it imparts

momentum into to the airflow in small velocity increments such that kinetic energy introduced into the airflow is minimal. The propeller therefore is being considered very seriously for many modern aircraft propulsion systems. Furthermore, the introduction of composite technology has also increased the popularity of the propeller by substantially increasing the strength to weight ratio.

1.2 DEVELOPMENT OF PROPELLER THEORY

While construction and implementation of propellers into propulsion systems continued for several decades from the turn of the 19th century, very few theoretical principles and analytical techniques were understood. It was not until 1909 with the publication of S. Drzewiecki's 'Des Helices Ariennes' [4] that an analytical approach to propeller design and analysis was taken. Drzewiecki reasoned that the blade could be divided into several small elements and the local velocities used to calculate the corresponding aerodynamic forces. This theoretical approach now commonly referred to as 'strip theory' or 'blade element theory' quickly became a key part of all analysis and design routines. However as Drzewiecki did not account for any induced velocities which had in fact been suggested earlier by W.J.M. Rankine and R.E. Froude [5,6], his methods did not agree well with experimental results. Corrective modifications were quickly suggested and later implemented by other authors.

An English engineer, H. Glauert considered that the velocity induced by the trailing vortex wake was significant and should be included in Drzewiecki's 'strip theory'. In 1922 Glauert published an analysis method based upon blade element, vortex and momentum theory [7]. Also at about this same time in Germany, A. Betz determined the trailing vortex structure corresponding to the optimum propeller efficiency [8,9]. That is, propeller design could be based solely on the condition that the trailing helicoidal vortex wake moves rearward with a constant "displacement" velocity.

As the velocity field induced by Betz's optimum trailing vortex wake is very complex an approximate representation was sought. L. Prandtl [10] and C.N. Lock [11] proposed approximate solutions and in 1929 S. Goldstein [12] obtained an exact potential flow solution to Betz's optimum vortex wake. Goldstein's solution was however, limited to

very light loadings and did not adequately represent off design trailing vortex wakes. Theodorsen [13,14,15] attempted to extend Goldstein's solution to heavy and static loadings but was unable to produce an exact method.

1.3 PRACTICAL APPROACH TO ANALYSIS AND DESIGN

The now classical propeller theory had been adequately developed by the end of the second world war but the computational ability was still lagging. As the iterative analysis and design routines were computationally intensive, several simplifying assumptions were necessary to minimize the manual computational time. The recent advent of the personal computer has now significantly reduced this computational time and has thus rendered the un-modified classical theory a practical approach. The classical propeller theory can now be efficiently implemented into practical design and analysis routines.

The accuracy of the analysis and design routines increases with the number of blade elements used and as the iterative tolerances are decreased. In the first instance the accuracy is limited only by the allotted run-time of the numerical routines, but there is also a finite error due to uncertainty in airfoil characteristics, assumption of a rigid helicoidal wake at off design conditions, and the presumption of an incompressible wake. Nevertheless, application of classical propeller theory to the design and analysis of light aircraft propellers is appropriate.

The classical propeller theory utilized in the analysis and design routines is discussed in Chapter two. The analysis and design routines are then outlined and verified in Chapters three and four respectively. In Chapter five the analysis and design routines are used to design an optimum propeller for a specific aircraft/engine configuration. Conclusions are presented in Chapter six.

Chapter 2

Propeller Theory

2.0 PROPELLER THEORY

2.1 FROUDE'S ACTUATOR DISC / MOMENTUM THEORY

2.1.1 INFLOW VELOCITY

Based upon Rankine's Classical Analysis [5], Froude proposed the actuator disc theory [6] as a model for the hypothetical flow through a plane-circular disc. The net pressure differential across the disc multiplied by the disc area can be equated to a forward thrust, which as shown by the conservation of momentum principle requires the downstream (slipstream) velocity to be greater than the upstream velocity. As a result the velocity at the disc must be greater than the upstream velocity by some small increment, often referred to as the inflow or induced velocity. It will be shown that this induced/inflow velocity is one half of the developed slipstream velocity.

If the flow along the streamlines is considered isentropic, incompressible and irrotational, the Navier-Stokes (energy) equations reduce to Bernoulli's equation;

$$\frac{P}{\rho} + \frac{|\bar{V}|^2}{2} = constant$$

As Bernoulli's equation is not valid across the discontinuity at the propeller disc, the flow field has been broken into two separate control volumes as shown in Figure 1. The entire flow field upstream of the propeller is taken as one control volume and the entire flow field downstream of the propeller as the second control volume. Applying Bernoulli's equation across both control volumes, the following two relations are obtained;

$$\frac{\rho U_1^2}{2} + P_1 = \frac{\rho U_2^2}{2} + P_2 \qquad (2.1a)$$

$$\frac{\rho U_3^2}{2} + P_2 + \Delta P = \frac{\rho U_4^2}{2} + P_4 \qquad (2.1b)$$

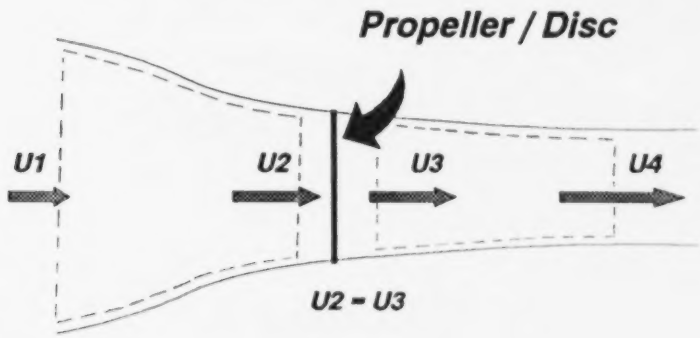

(a) Control Volumes

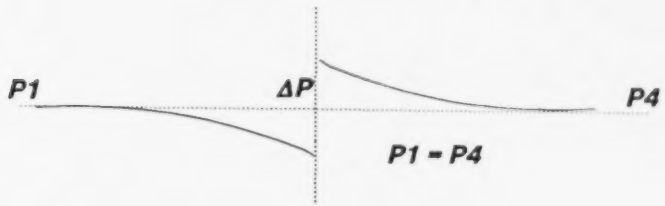

(b) Pressure along center line

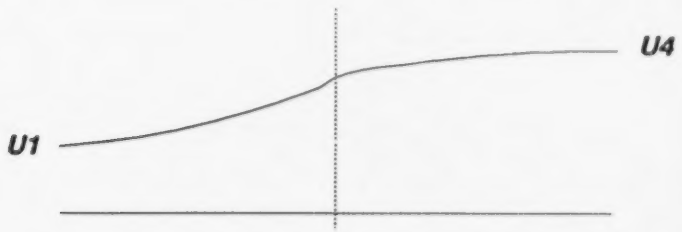

(c) Velocity distribution

Figure 1, Momentum - Bernoulli / Froude

The control points 3 and 4 are taken infinitely far upstream and infinitely far downstream respectively, such that P_4 and P_1 are equal. It is also assumed that the velocity is uniform through the disc (ie. $U_2=U_3$). An expression for ΔP is then found by solving equations 2.1a and 2.1b simultaneously;

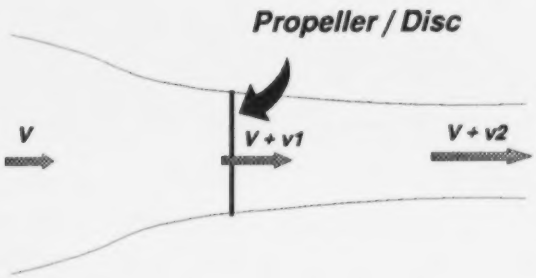

Figure 2, Axial Inflow Velocities - Momentum

$$\Delta P = \frac{\rho}{2}(U_4^2 - U_1^2)$$

and rewritten in terms of the velocities as shown in Figure 2:

$$\Delta P = \frac{\rho}{2}((V + v_2)^2 - V^2)$$

$$= \rho v_2 (V + \frac{1}{2} v_2)$$

This pressure differential (ΔP) across the propeller disc is representative of the forward thrust which can be determined by:

$$T = \Delta P \cdot A$$

$$= \rho \cdot v_2 \cdot (V + \frac{1}{2} v_2) \cdot A \qquad (2.2)$$

Furthermore as linear momentum is conserved across the entire propeller flow field, the forward thrust is also determined by the rate of change of linear momentum.

$$T = \frac{d}{dt}(momentum)$$

$$= \dot{m} \cdot (V + v_2) - \dot{m} \cdot V$$

$$= \dot{m} \cdot v_2$$

$$= \rho \cdot A \cdot (V + v_1) \cdot v_2 \qquad (2.3)$$

$$where, \quad \dot{m} = \rho \cdot A \cdot (V + v_1)$$

A relation between the axial inflow velocity at the propeller disc and the axial velocity increment in the far downstream wake is determined by equating equation 2.2 with equation 2.3;

$$\rho \cdot (V + v_1) \cdot v_2 \cdot A = \rho \cdot (V + \frac{1}{2} v_2) \cdot v_2 \cdot A$$

$$\Rightarrow \quad v_1 = \frac{1}{2} v_2 \qquad (2.4)$$

For lightly loaded propellers the angular (rotational) inflow velocity, ω_1, is relatively small compared with the axial inflow velocity, v_1. Nevertheless it is still necessary to obtain a relationship between the angular inflow velocity, ω_1, at the propeller disc and the incremental angular velocity, ω_2, in the far wake (Figure 3). As the incremental axial velocity in the far wake, v_2, is twice the axial inflow velocity at the propeller, v_1, and the density is assumed to be constant, continuity requires the ratio of the slipstream radius, R_2, in the far wake to the disc radius, R_1, at the propller to be

$$\pi \cdot R_1^2 \cdot (V + v_1) = \pi \cdot R_2^2 \cdot (V + v_2)$$

$$\Rightarrow \quad \frac{R_2^2}{R_1^2} = \frac{V + v_1}{V + 2v_1}$$

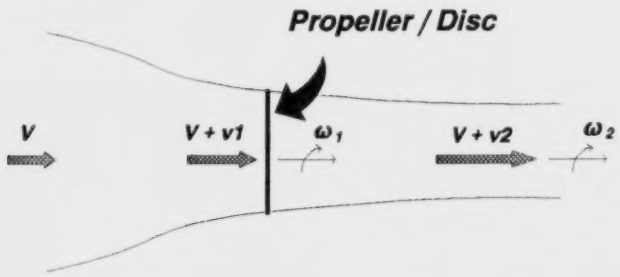

Figure 3, Rotational Inflow Velocities - Momentum

Also from the conservation of angular momentum the ratio of the slipstream radius, R_2, in the far wake to the disc radius, R_1, at the propller is given by

$$\dot{m} \cdot R_1^2 \cdot \omega_1 = \dot{m} \cdot R_2^2 \cdot \omega_2$$

$$\rightarrow \quad \frac{R_2^2}{R_1^2} = \frac{\omega_1}{\omega_2}$$

Equating the radius ratios as determined by continuity and conservation of angular momentum, the angular inflow velocity , ω_1 is then given by

$$\omega_1 = \frac{1}{2}\omega_2 * \frac{1}{1-(\frac{1}{2+v_1/V})}$$

When the velocity, V, is relatively large with respect to the axial inflow velocity, v_1,

$$\omega_1 \approx \omega_2 \qquad (2.5a)$$

However when the velocity, V, is relatively small with respect to the axial inflow velocity, v_1;

$$\omega_1 \approx \frac{1}{2}\omega_2 \qquad (2.5b)$$

Equation 2.5b is considered in the literature to be generally more representative than equation 2.5a and has therefore been utilized herein.

Equations 2.4 and 2.5b are very useful in that the rotational and axial incremental velocities in the far wake can be eliminated from the equations for thrust and torque. The variable v_2 can be eliminated from the expression for thrust in equation 2.3 and the axial inflow velocity can be shown to be proportional to the thrust and inversely proportional to both the propeller disc area and forward velocity.

$$T = \rho \cdot A \cdot (V + v_1) \cdot v_2$$

$$\approx 2 \cdot \rho \cdot A \cdot v_1 \cdot V \qquad \textit{where,} \quad v_2 = 2v_1 \;\; ; \; v_1 << V$$

$$\Rightarrow \quad v_1 \approx \frac{T}{2 \cdot \rho \cdot V \cdot A} \propto \frac{T}{V \cdot A}$$

Also the variable ω_2 can be eliminated in the expression for torque. The rotational inflow velocity is then shown to be proportional to the torque and inversely proportional to both the propeller disc area and forward velocity.

$$Q = \frac{d}{dt}(\textit{Angular Momentum})$$

$$= \dot{m} \cdot R_2^{\,2} \cdot \omega_2$$

$$= \rho \cdot A \cdot (V + v_1) \cdot R_2^{\,2} \cdot \omega_2 \qquad \textit{where,} \quad \dot{m} = \rho \cdot A \cdot (V + v_1)$$

$$\approx \rho \cdot A \cdot V \cdot R_1^{\,2} \cdot \omega_1 \qquad \textit{where,} \quad \omega_2 = 2\omega_1 \;\; ; \; R_2^{\,2} = \frac{1}{2} R_1^{\,2} \;\; ; \; v_1 << V$$

$$\Rightarrow \quad \omega_1 \approx \frac{Q}{\rho \cdot A \cdot R_1^{\,2} \cdot V} \propto \frac{Q}{V \cdot A}$$

2.1.2 IDEAL EFFICIENCY (FROUDE'S ACTUATOR DISC)

Froude [6] defined the ideal efficiency of the actuator disc as the ratio of developed output power to the input power:

$$\eta = \frac{\textit{Useful Power}}{\textit{Input Power}} = \frac{T \cdot V}{T \cdot (V + v_1)} = \frac{1}{1 + \frac{v_1}{V}}$$

The highest efficiency is therefore obtained when the forward velocity V is maximized and the axial inflow velocity v_1 is minimized. The forward speed is normally specified but the axial inflow velocity can be manipulated somewhat. The axial inflow velocity, v_1, is inversely proportional to the disc area so in the first instance it is minimized and the efficiency optimized by utilizing the largest possible propeller diameter.

2.1.3 EXTENSION OF ACTUATOR DISC THEORY

The actuator disc model is very idealized but nonetheless it does provide some good indicators on how to maximize the efficiency of a practical propeller. That is for a given required thrust, the propeller diameter should be maximized in order to minimize the axial inflow velocity. Also actuator disc theory is based on the assumption that the rotational inflow velocity is negligible with respect to the axial inflow velocity. It is therefore necessary to minimize the rotational inflow velocity which in the first instance is accomplished by maximizing the propeller diameter. Furthermore as both the rotational and axial inflow velocities are inversely proportional to the forward velocity, the inflow velocities are minimized and hence the efficiency maximized by maximizing the forward velocity.

The actuator disc theory is simple and hence appealing but in itself is not adequate to model a practical propeller. The actuator disc theory assumes an infinite number of blades but most propellers have only two to three blades. Blade element theory, vortex theory, and Prandtl's semi-infinite plate analogy can all be combined with actuator disc theory to model propellers with finite number of blades more accurately.

2.2 BLADE ELEMENT THEORY

Blade element theory as first introduced by Drzewiecki is illustrated in Figure 4. The relative velocity, W, is simply calculated as the vector sum of the forward velocity, V, and the rotational velocity, Ωr. The angle of attack, α, is calculated as the difference between the blade angle, β, measured from the plane of rotation to the zero lift line and the relative velocity angle, ϕ. From the angle of attack the lift and drag characteristics of the airfoil are determined and the local thrust and torque calculated. Implicit within the model is the assumption that the blade can be considered as several independent airfoil sections and that the total thrust and torque can be determined by a summation of all the local thrust and torque values.

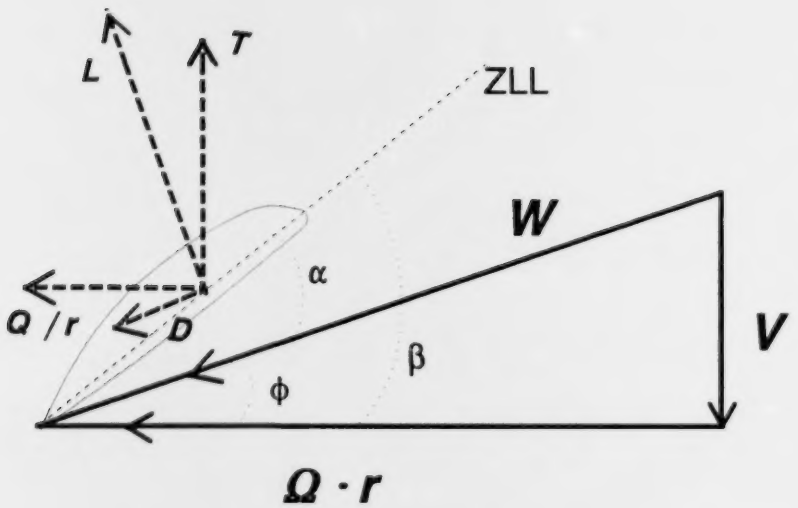

Figure 4, Blade Element Theory

The thrust and torque of a blade element are given by:

$$T_e = L_e \cdot \cos(\phi) - D_e \cdot \sin(\phi)$$

$$= L_e \cdot \cos(\phi) \cdot (1 - \epsilon \cdot \tan(\phi)) \quad , \epsilon = \frac{D_e}{L_e}$$

$$Q_e = [L_e \cdot \sin(\phi) + D_e \cdot \cos(\phi)] \cdot r$$

$$= [L_e \cdot \sin(\phi) \cdot (1 + \frac{\epsilon}{\tan(\phi)})] \cdot r$$

$$Thrust = \int_{r_o}^{R} \frac{dT_e}{dr} \cdot dr \qquad Torque = \int_{r_o}^{R} \frac{dQ_e}{dr} \cdot dr$$

Since Drzweicki's blade element model did not account for any inflow velocities whatsoever, it is not surprising that it did not agree well with experiment. Momentum theory shows that there must be an inflow velocity if any thrust is developed. Modern blade element theory therefore takes the inflow velocities into account which as shown in Figure 5 are represented by:

$$v_1 = a \cdot V \quad ; \quad \omega_1 = a' \cdot \Omega$$

The net result of having included the inflow velocities into the blade element model is an increased axial velocity and a decreased effective rotational velocity. Also, the angle ϕ increases which has the effect of reducing the angle of attack, α.

$$\alpha = \beta - \phi \qquad (\beta \textit{ is fixed for a particular propeller})$$

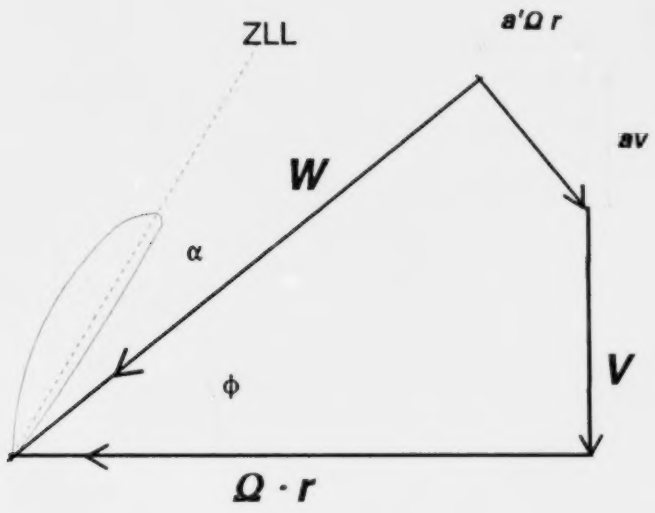

Figure 5, Modified Blade Element Theory

The magnitude and angle of the resultant velocity vector are then calculated as the vector sum of the forward, rotational, and inflow velocities;

$$W = V_{rel} = \sqrt{[V(1+a)]^2 + [\Omega r(1-a')]^2}$$

$$\phi = \tan^{-1}[\frac{V(1+a)}{\Omega r(1-a')}]$$

The blade element procedure as introduced by Drzweicki is still valid as only the angle of attack and relative velocity are modified by the induced velocities.

2.3 CONDITION FOR MINIMUM INDUCED LOSS

The concept of minimum induced loss propellers was introduced by A. Betz [8,9] in 1919. He showed that the induced losses are minimized if the trailing vortex wake moves rearward with a constant displacement velocity, v', and in the form of a rigid helicoid.

Consider the blade element shown in Figure 6, at a distance r from the axis of rotation with an axial velocity, V, and tangential velocity, $\Omega \cdot r$. If the blade is considered frictionless and velocities induced by the trailing vortices are ignored, the propeller would experience no energy loss and the resultant force, dF, would be due entirely to the airfoil lift. The thrust and torque components can then be expressed in terms of the circulation, Γ.

$$dT = \rho \cdot \Gamma \cdot \Omega \cdot r \cdot dr$$

$$dQ = \rho \cdot \Gamma \cdot V \cdot r \cdot dr$$

Now if an infinitesimally small circulation, $\Delta\Gamma$, is applied at each blade element the elemental thrust would increase by ΔdT, the elemental torque would increase by ΔdQ, and the blade element efficiency would be given by

$$\eta_e = \frac{V \cdot (dT + \Delta\, dT)}{\Omega \cdot (dQ + \Delta\, dQ)} = \frac{V \cdot dT + V \cdot \Delta\, dT}{\Omega \cdot dQ + \Omega \cdot \Delta\, dQ}$$

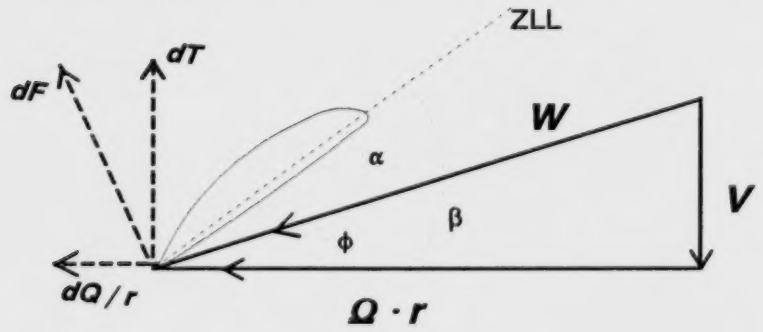

Figure 6, Idealized Blade Element - No Losses

For maximum efficiency the distribution of circulation about the propeller blade must be optimum, which as shown by Glauert [7] is realized when the ratio of the output power increment, $V \cdot \Delta dT$, to the input power increment, $\Omega \cdot \Delta dQ$, is constant along the blade.

$$\kappa_e = \frac{V \cdot \Delta dT}{\Omega \cdot \Delta dQ} = constant$$

To simplify the above discussion the blade element was considered frictionless and inflow velocities were not accounted for. Any practical propeller however, will have some friction represented in the form of aerodynamic drag and the inflow velocities are significant. The frictionless blade element model shown in Figure 6 is easily modified to include frictional effects by introducing a drag component as shown in Figure 7. The addition of friction results in a thrust reduction and torque increase at each blade element but as the optimum efficiency is still realized when the increment of work is of the same magnitude as the increment of power, the ratio κ is still constant along the propeller blade. Also, a velocity, w_i, is induced by the trailing vortex wake and as shown in Figure 8 it can be represented in terms of axial and radial inflow velocities. According to Glauert [7] and Munk [16] these inflow velocities can be incorporated into the expressions for incremental thrust and incremental torque.

$$\Delta dT = \rho \cdot \Delta\Gamma \cdot (\Omega - \omega_1) \cdot r \cdot \Delta r$$

$$\Delta dQ = \rho \cdot \Delta\Gamma \cdot (V + v_1) \cdot r \cdot \Delta r$$

The structure of the trailing vortex wake corresponding to optimum efficiency is arrived at by considering the incremental thrust and torque expressions in light of the constant κ ratio.

$$\kappa = \frac{V \cdot \Delta dT}{\Omega \cdot \Delta dQ} = \frac{V \cdot (\Omega - \omega_1)}{\Omega \cdot (V + v_1)} = constant$$

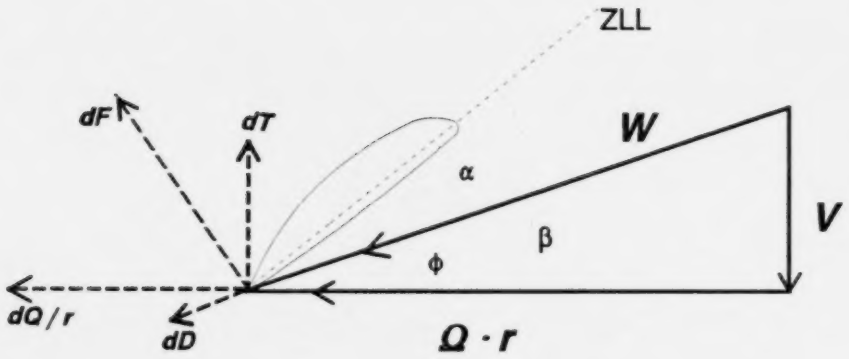

Figure 7, Optimum Wake - Frictional Considerations

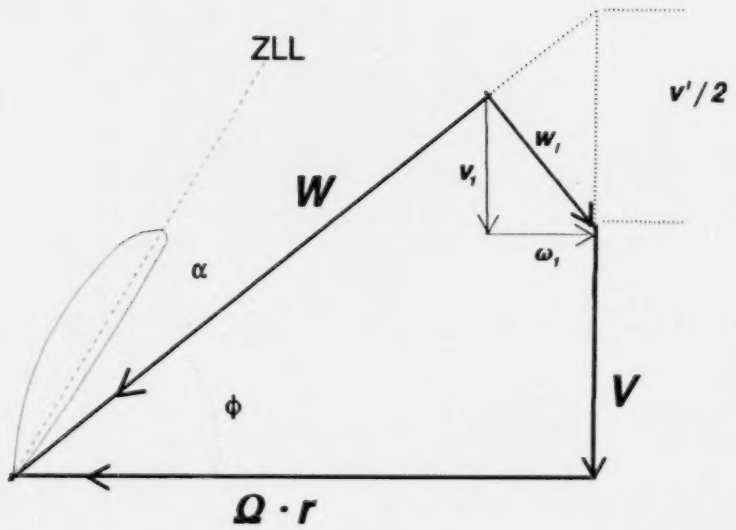

Figure 8, Inflow Velocities Induced by the Vortex Wake

Upon applying the principle of similar triangles to the velocity diagram in Figure 8,

$$\frac{V + v'/2}{\Omega \cdot r} = \frac{V + v_1}{(\Omega - \omega_1) \cdot r}$$

the expressions can be rearranged and solved for v'.

$$\Rightarrow V + v'/2 = \frac{V}{\kappa}$$

As the forward velocity, V, and ratio κ are constant along the blade, the displacement velocity, v', must also be constant.

2.3.1 OPTIMUM VORTEX WAKE

The above arguments demonstrate that for an optimum propeller the displacement velocity must be constant along the propeller radius. As shown in Figure 9 the vortex filaments leaving the propeller blades appear to move rearwards along the propeller axis with velocity, v', and lie on a screw surface of constant pitch.

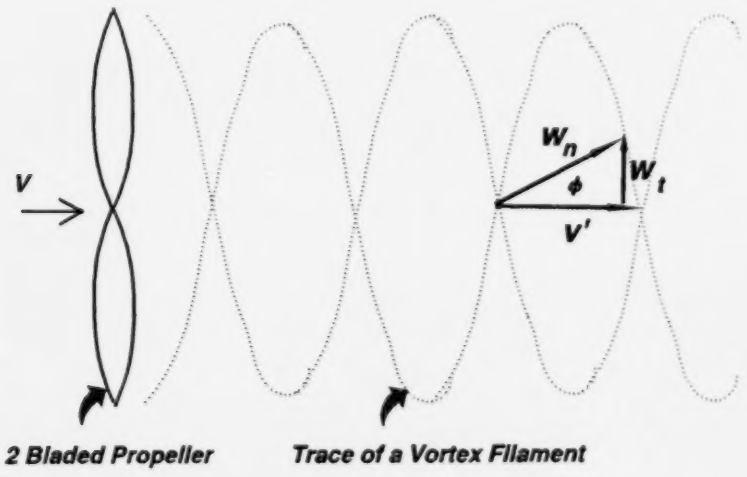

Figure 9, Vortex Filament Trace

Vortex filaments shed from each blade element combine to form helocoidal trailing vortex sheets. These vortex sheets move perpendicular to themselves and induce both axial and radial velocity components to the slipstream. At the propeller these induced velocities, v_i and ω_i, form the resultant induced velocity vector w_i, which acts perpendicular to both the vortex sheets and the relative velocity vector, W. Far downstream of the propeller the slipstream moves normal to the vortex sheets with velocity, w_n. As shown in Figure 9 the slipstream velocity, w_n, and its rotational component, w_t, are readily calculated in terms of the constant displacement velocity, v'.

2.3.2 OPTIMUM BLADE CIRCULATION

Stepniewski [17] has shown that for a lightly loaded propeller the slipstream velocity at radius r is influenced only by the blade circulation at radius r. Therefore having determined the slipstream velocity corresponding to the optimum vortex wake (v'=const), the optimum blade element circulation at the corresponding blade radius is readily determined.

Radial variation of the blade vortex strength Γ corresponding to an optimum propeller, is calculated by setting the total bound circulation, $B\Gamma$, at the blade radius r equal to the circulation about the slipstream tube of the same radius [25].

$$B \cdot \Gamma = \oint w_t \, dl = 2 \cdot \pi \cdot r \cdot w_t \tag{2.6}$$

As shown in Figure 9 the slipstream rotational velocity velocity, w_t, corresponding to the optimum vortex wake (v'=const) is given by

$$\begin{aligned} w_t &= w_n \cdot \sin(\phi) \\ &= [v' \cdot \cos(\phi)] \cdot \sin(\phi) \end{aligned} \tag{2.7}$$

Substituting equation 2.7 into equation 2.6, the optimum blade circulation is given by

$$B \cdot \Gamma = 2 \cdot \pi \cdot r \cdot v' \cdot \cos(\phi) \cdot \sin(\phi)$$

2.4 PRANDTL'S MOMENTUM LOSSES

The optimum vortex wake of constant displacement velocity was utilized in the previous section to determine the optimum design blade circulation. As this optimum circulation was calculated in terms of the constant displacement velocity, radius, and angle of attack only, it was not necessary to actually calculate the slipstream velocity. However to evaluate the momentum equations the actual slipstream velocity must be determined.

Prandtl visualized the trailing vortex sheets as rigid plates moving within a fluid and thereby inducing a velocity to the fluid. If the spacing between these vortex sheets or plates is infinitely small the velocity imparted to the slipstream would be constant along the radius, and is easily calculated in terms of the constant displacement velocity. However, when the number of blades become finite the induced axial velocity tends to fall off towards the tip and as shown in Figure 10 actually approaches zero at the tip. To account for these "tip losses" a radially graded correction factor must be applied to the slipstream velocity field.

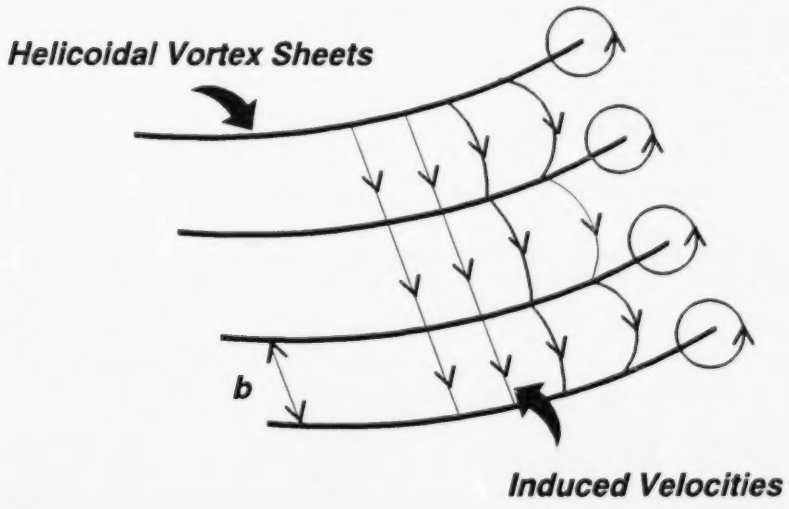

Figure 10, Induced Velocity Distribution (Prandtl)

Prandtl [10] has given an approximate method for estimating the tip losses due to the small radial velocities. He modelled the vortex sheets as semi-infinite plates spaced at regular intervals moving in a fluid with velocity w_n. A. Glauert [7] also develops this theory and as shown in Figure 11, the velocity distribution is approximated with the tip loss factor F.

$$F = \frac{2}{\pi}\cos^{-1}(e^{-f}) \qquad \textit{where,} \quad f = \pi\frac{x}{b}$$

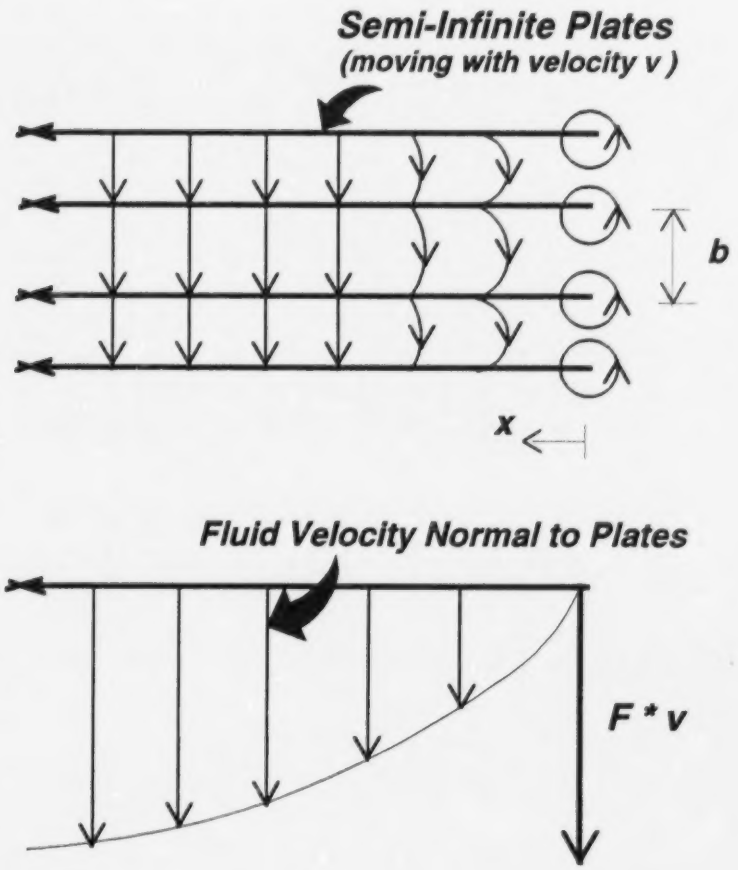

Figure 11, Velocity Distribution, Semi-Infinite Plates

For a propeller with B number of blades, the distance between the trailing vortex sheets is given by

$$b = \frac{2 \cdot \pi \cdot R}{B} \cdot \tan(\phi) \cdot \cos(\phi)$$

Ideally the angle ϕ is found with regard to the full velocity field including the induced velocities. However as the inflow velocities are relatively small compared to the forward and rotational velocity for a lightly loaded propeller, the angle ϕ can be approximated as a function of the forward and rotational velocities only. The sheet spacing is then

$$b = \frac{2 \cdot \pi \cdot R}{B} \frac{\lambda}{\sqrt{\lambda^2 + 1}} \qquad \textit{where,} \quad \lambda = \frac{V}{\Omega R}$$

and Prandtl's momentum / tip loss factor is determined by

$$f = \frac{B}{2} \frac{\sqrt{\lambda^2 + 1}}{\lambda} (1 - \frac{r}{R})$$

$$F = \frac{2}{\pi} \cos^{-1}(e^{-f})$$

Prandtl's method of estimating the tip losses, using the analogy of an infinite number of plates is very practical but is only approximate. S.Goldstein [12] developed a more accurate analysis of the problem, in that he solved for the potential flow around the helicoidal vortex sheets. He developed the method to the point that the circulation along the blades as a function of radius, r, and speed ratio, λ, could be determined for 2 and 4 bladed propellers. This is very accurate but it involves several complex modified Bessel functions which can only be solved for infinitely light loadings and unfortunately does not account for a finite hub radius. C. Lock [11] attempted to correct for the shortcomings of Goldstein's method, and he did manage to extend it to include moderate loadings, finite hub radius, and various numbers of blades. This method commonly referred to as the Goldstein-Lock method does work but reference to empirical tables is

required. Prandtl's simple tip loss method is much easier to incorporate into a design procedure than the Goldstein-Lock method and for a large number of blades operating at low advance ratios the solutions agree well. However as indicated by Glauert [7], the discrepancy between Prandtl's and the more exact Goldstein-Lock solution increases as the number of blades decreases and/or the advance ratio increases.

The deviation of Prandtl's approximation from Goldstein's exact solution is demonstrated by means of the optimum circulation distribution.

$$G = \frac{B \cdot \Omega \cdot \Gamma}{2 \cdot \pi \cdot V \cdot v'}$$

Goldstein has determined numerically, exact values for the circulation function corresponding to two and four bladed lightly loaded propellers [12]. Prandtl on the other hand has approximated the circulation function by considering the bound circulation about the blade and the corresponding circulation in the wake. The circulation is given by

$$B \cdot \Gamma = 2 \cdot \pi \cdot r_s \cdot v' \cdot \cos(\phi) \cdot \sin(\phi) \cdot F$$

and assuming that the inflow velocities are much smaller than the forward and rotation velocities

$$\sin(\phi) \approx \frac{1}{\sqrt{\chi^2 + 1}}$$

$$\cos(\phi) \approx \frac{\chi}{\sqrt{\chi^2 + 1}}$$

$$\textit{where}\ , \quad \chi = \frac{\Omega R}{V}$$

The optimum circulation function as approximated by Prandtl is then

$$G = \frac{B \cdot \Omega \cdot \Gamma}{2 \cdot \pi \cdot V \cdot v'} = F \frac{\chi^2}{\chi^2 + 1}$$

The two solutions are shown graphically in Figure 12 for both a two and four bladed propeller operating at an advance ratio of 0.628. It is seen that agreement between the two methods is better for the four bladed propeller but also as shown in Table 1, the spacing between the trailing vortex sheets shed by the four bladed propeller is less than that of the two bladed propeller. This result indicates that the vortex sheet spacing has a strong affect on the accuracy of Prandtl's approximation. To further illustrate this concept, the two solutions shown in Figure 13 were obtained for a two bladed propeller operating at various advance ratios. A lower advance ratio, which corresponds to a smaller vortex sheet spacing as shown in Table 2, produces a better agreement between Prandtl's and Goldstein's solutions. If an 18% deviance between Goldstein's exact solution and Prandtl's approximate solution is acceptable then the vortex sheet spacing should not be greater than the propeller radius. Larabee [18] very eloquently concludes that "Goldstein's results may be interpreted as confirming the Betz-Prandtl approximation whenever the vortex sheet spacing is less than the propeller radius".

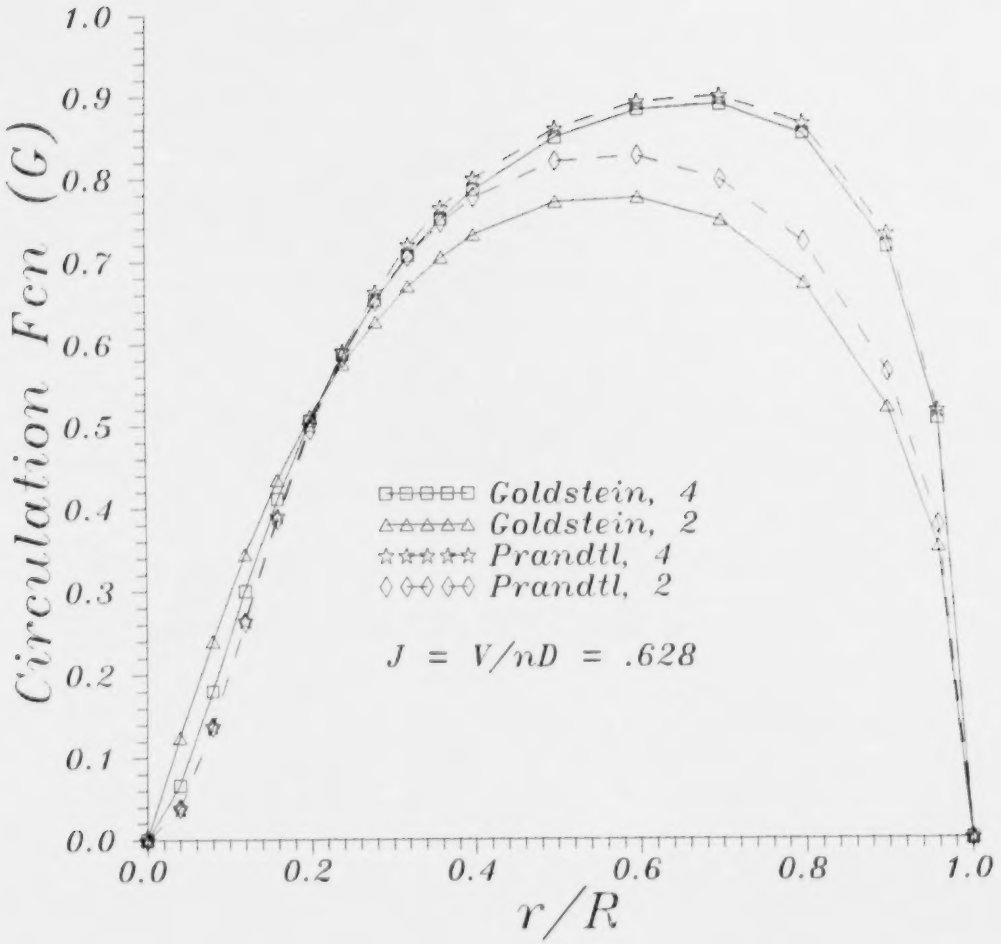

Figure 12, Goldstein's Exact and Prandtl's Approximate Circulation Functions for 2 and 4 Blades

Table 1, Optimum Circulation Distribution for 2 and 4 Bladed Propellers at an Advance Ratio of 0.628

Number of Blades (B)	Vortex Sheet Spacing (b/R) *	Percent Error (maximum) **
2	0.62	6.5 (@ r/R=0.6)
4	0.31	1.1 (@ r/R=0.6)

Table 2, Optimum Circulation Distributions for a 2 Bladed Propeller

Advance Ratio (J = V/nD)	Vortex Sheet Spacing (b/R) *	Percent Error (maximum) **
1.57	1.40	31.7 (@ r/R=0.7)
1.05	1.00	17.9 (@ r/R=0.67)
0.785	0.76	10.0 (@ r/R=0.63)
0.628	0.62	6.5 (@ r/R=0.6)
0.392	0.39	1.7 (@ r/R=0.5)

* $\frac{b}{R} = \frac{2\pi}{B}\frac{\lambda}{\sqrt{\lambda^2+1}}$ *where,* $\lambda = \frac{J}{\pi}$

** $\%err = \frac{G_{Prandtl} - G_{Goldstein}}{G_{Goldstein}} * 100$

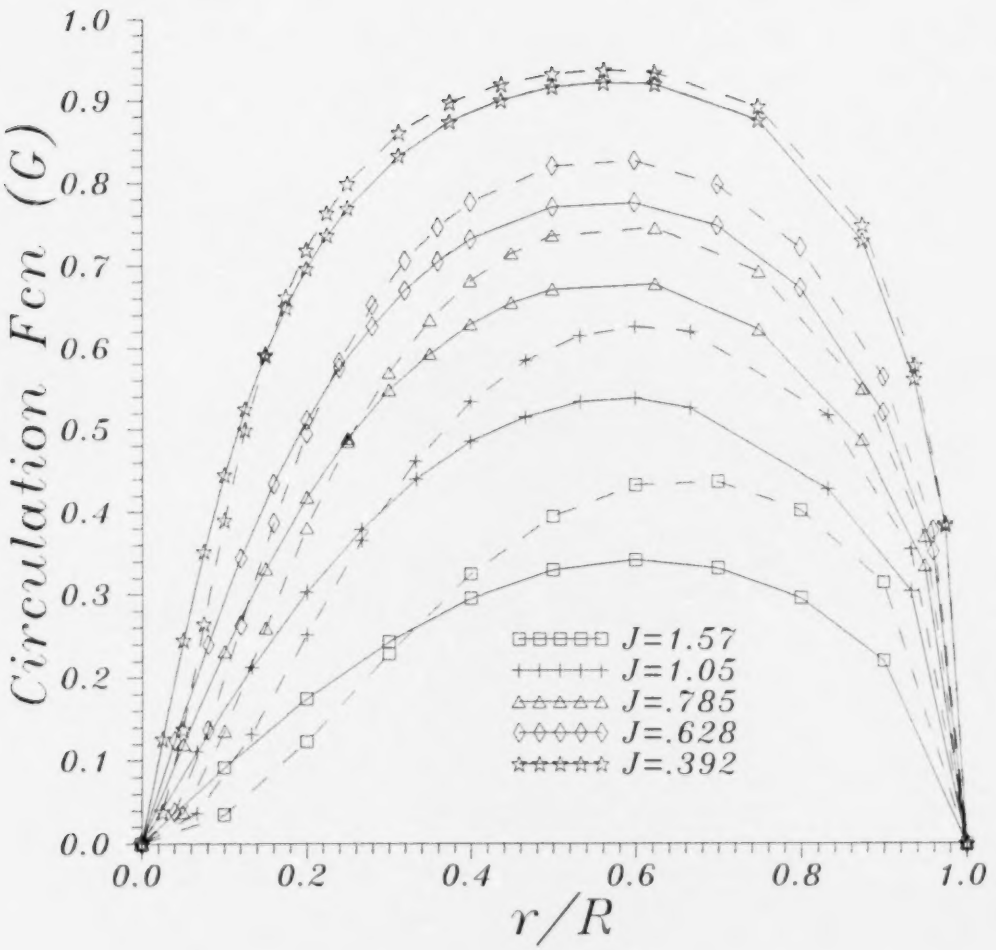

Figure 13, Goldstein's Exact (Solid Lines) and Prandtl's Approximate (Dashed Lines) Circulation Functions for 2 Blades

2.5 FLOW FIELD AROUND AN AXI-SYMMETRIC BODY

Interference due to an engine nacelle and/or propeller hub should be accounted for as the local flow field can be modified quite significantly. As shown in Figure 14, the incoming air is forced to flow around the nacelle which has the effect of introducing a radial component into the free stream axial velocity. The axial velocity component is thus reduced and its magnitude in relation to the free-stream axial velocity becomes of importance. The radial velocity component may have some effect on the blade aerodynamics but in this instance it is ignored. Furthermore it is assumed that the propeller is mounted far enough upstream of the main nacelle that it does not further modify the generalized flow field as imposed by the nacelle.

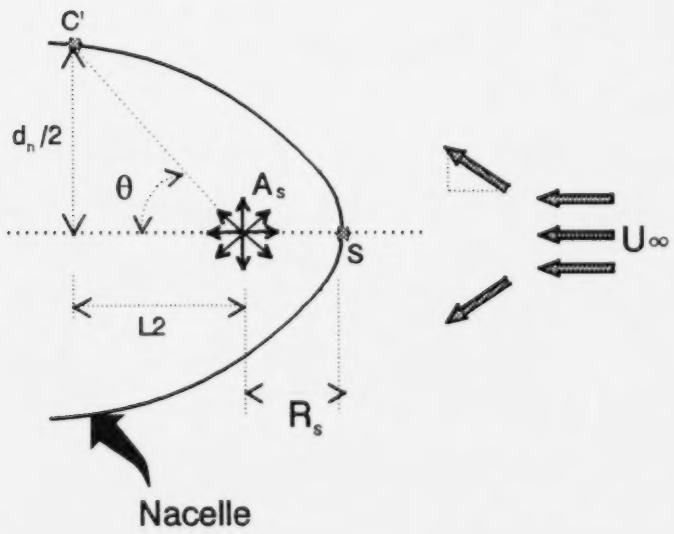

Figure 14, Nacelle Interference

The flow field around most engine / nacelle configurations is sufficiently represented by a 3-D, axi-symmetric, potential flow analysis. A. Breeze-Stringfellow [19] has presented one such method, by which the flow field around specific axi-symmetric bodies is numerically determined. This numerical approach is appealing because the exact coordinates of the nacelle are utilized and the flow field is calculated very precisely. However, the numerical solution is very complex and as the nacelles on most light aircraft are not axi-symmetric the numerical model may not be fully representative and hence is often not warranted. A more efficient approach is to assume an generalized axi-symmetric body, based upon the coordinates of the nacelle at one point far downstream of the stagnation point. An approximate solution to the 3-D flow field is then arrived at relatively easily.

Superposition of a 3-D potential source onto a uniform velocity field as shown in Figure 14, models the axi-symmetric flow over a semi-infinite body of revolution [20]. The potential function (ϕ) for this combined flow, written in spherical coordinates is:

$$\Phi(R,\theta,\psi) = U_\infty \cdot R \cdot \cos(\theta) - \frac{A_s}{R}$$

The velocity at any spherical point (R, θ, Φ) may be expressed in terms of the potential function and determined as follows:

$$U_R = \frac{\partial \Phi}{\partial R} = U_\infty \cos(\theta) + \frac{A_s}{R^2} \tag{2.8}$$

$$U_\theta = \frac{1}{R}\frac{\partial \Phi}{\partial \theta} = -U_\infty \sin(\theta) \tag{2.9}$$

$$U_\psi = \frac{1}{R \cdot \sin(\theta)}\frac{\partial \Phi}{\partial \psi} = 0 \tag{2.10}$$

At the stagnation point S ($\theta=\theta_s=\pi$), the velocity is zero and from equation 2.8, the location of the stagnation point is found to be

$$R_s = \sqrt{\frac{A_s}{U_\infty}}$$

Also if at a point C' the body is nearly cylindrical, the volume flow rate through a cross section is

$$q = \frac{\pi}{4} \cdot d_n^2 \cdot U_\infty$$

from which the source strength is found as

$$A_s = \frac{q}{4\pi} = \frac{d_n^2}{16} U_\infty$$

The radial and angular velocity components are then written as;

$$U_r = \frac{\partial \Phi}{\partial R} = U_\infty [\cos(\theta) + \frac{d_n^2}{16 R^2}]$$

$$U_\theta = \frac{1}{R} \frac{\partial \Phi}{\partial \theta} = -U_\infty \cdot \sin(\theta)$$

and the resultant axial component of the velocity is;

$$\frac{U_x}{U_\infty} = -\frac{U_r}{U_\infty} \cos(\pi - \theta) - \frac{U_\theta}{U_\infty} \cos(\theta - \pi/2)$$

$$\frac{U_x}{U_\infty} = -[\cos(\theta) + \frac{d_n^2}{16 R^2}] \cos(\pi - \theta) + \sin(\theta) \cos(\theta - \pi/2)$$

Chapter 3

Analysis

3.0 ANALYSIS

The essential function of the analysis routine is to determine the axial and rotational inflow velocities at the propeller disc. Once the velocity at the propeller disc is known, the velocity in the fully developed slipstream can be calculated as well as the produced thrust and required power.

The magnitude of the inflow velocities induced by the trailing vortex wake varies according to the wake structure and dynamics. Several precise models for the trailing vortex wake have been suggested [1,21] but they are very complex, require extensive computer facilities, and are very time intensive. An efficient approach is to assume a rigid helicoidal wake [8,9,10] and indirectly solve for the inflow velocities using the conservation of momentum and blade element theory.

3.1 DERIVATION OF GOVERNING EQUATIONS

The velocity component tangential to the rotating propeller blade is a function of both the rotational velocity and the blade radius. The governing equations must therefore be assessed at each blade element and then integrated over the entire blade. The thrust and torque at each blade element are found by applying the momentum principle across the corresponding propeller flow field as shown in Figure 15.

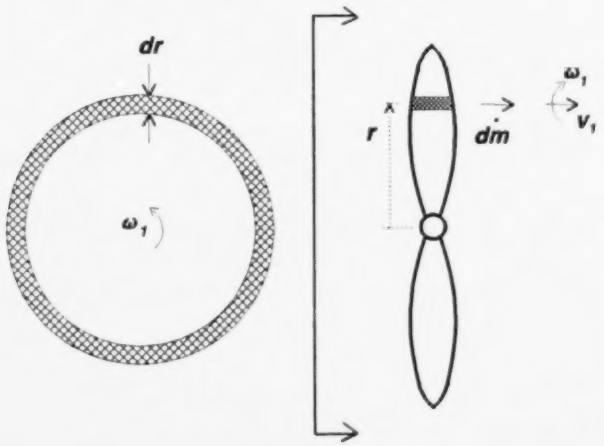

Figure 15, Momentum - Blade Element Considerations

By conservation of linear momentum the thrust is

$$dT = \dot{dm} \cdot v_2 \cdot F \tag{3.1}$$

and similarly by conservation of angular momentum the torque is

$$dQ = r \cdot \dot{dm} \cdot (r \cdot \omega_2) \cdot F \tag{3.2}$$

As the exact structure of the trailing vortex wake is very difficult to ascertain it is simply assumed to be helicoidal. Therefore the momentum loss factor F as given by Prandtl is also assumed to be appropriate.

$$F = \frac{2}{\pi} \cdot \cos^{-1}(e^{-f})$$

$$f = \frac{B \cdot (1 - r/R)}{2 \cdot \sin(\phi_T)} \qquad \textit{where,} \quad \phi_T = \phi \textit{ at blade tip}$$

In this instance the factor f is determined with respect to the angle ϕ_T, corresponding to the actual relative velocity vector, W. Furthermore as the momentum loss factor F is determined with respect to the axis perpendicular to the vortex sheets as shown in Figure 16, it must be applied to the torque as well as the thrust equations.

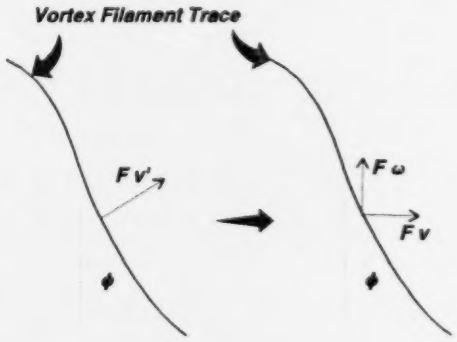

Figure 16, Momentum Loss Factor w.r.t. Vortex Sheets

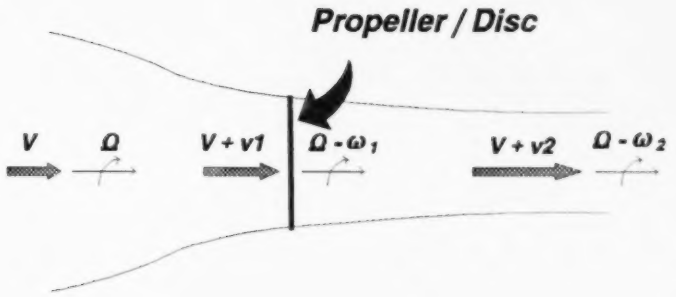

Figure 17, Wake and Inflow Velocities

The incremental velocities v_2 and ω_2 taken in the far wake as shown in Figure 17, are represented in terms of the inflow factors a and a' by;

$$a = \frac{v_1}{V} \; ; \quad v_1 = \frac{1}{2} v_2 \qquad \Rightarrow v_2 = 2aV$$

$$a' = \frac{\omega_1}{\Omega} \; ; \quad \omega_1 = \frac{1}{2} \omega_2 \qquad \Rightarrow \omega_2 = 2a'\Omega$$

and the mass flow rate calculated at the propeller disc is given by

$$\dot{dm} = V \cdot (1 + a) \cdot \rho \cdot 2 \cdot \pi \cdot r \cdot dr$$

Equations 3.1 and 3.2 can then be rewritten as

$$dT = 4 \cdot \pi \cdot \rho \cdot r \cdot V^2 \cdot a \cdot (1 + a) \cdot F \cdot dr \tag{3.3}$$

$$dQ = 4 \cdot \pi \cdot \rho \cdot r^3 \cdot \Omega \cdot V \cdot (1 + a) \cdot a' \cdot F \cdot dr \tag{3.4}$$

An additional set of expressions for the incremental thrust and torque are arrived at through blade element considerations. The blade element lift and drag coefficients as shown in Figure 18, are equated as follows

$$dT = dL \cdot \cos(\phi) - dD \cdot \sin(\phi)$$

$$= \frac{1}{2} \cdot \rho \cdot W^2 \cdot C \cdot B \cdot (C_L \cdot \cos(\phi) - C_D \cdot \sin(\phi)) \cdot dr \tag{3.5}$$

$$dQ = r \cdot (dL \cdot \sin(\phi) + dD \cdot \cos(\phi))$$

$$= \frac{1}{2} \cdot \rho \cdot W^2 \cdot C \cdot B \cdot r \cdot (C_L \cdot \sin(\phi) + C_D \cdot \cos(\phi)) \cdot dr \tag{3.6}$$

where, $dL = C_L \cdot \frac{1}{2} \cdot \rho \cdot W^2 \cdot C \cdot dr$

$$dD = C_D \cdot \frac{1}{2} \cdot \rho \cdot W^2 \cdot C \cdot dr$$

$$\phi = \tan^{-1}\left(\frac{V \cdot (1 + a)}{r \cdot \Omega \cdot (1 - a')}\right)$$

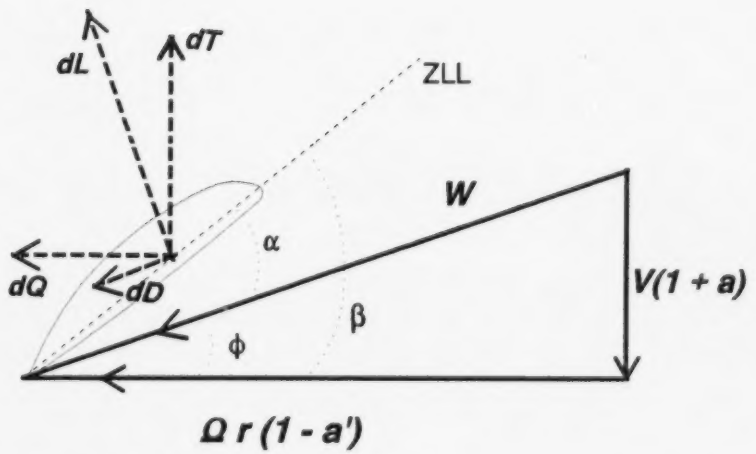

Figure 18, Blade Element Theory

The incremental thrust as determined by momentum considerations must equate to that determined by blade element considerations.

$$dT = 4 \cdot \pi \cdot \rho \cdot r \cdot V^2 \cdot a \cdot (1 + a) \cdot F \cdot dr = \frac{1}{2} \cdot B \cdot \rho \cdot W^2 \cdot C \cdot (C_L \cdot \cos(\phi) - C_D \cdot \sin(\phi)) \cdot dr$$

$$\textit{where,} \quad W = V_{rel} = \frac{V \cdot (1 + a)}{\sin(\phi)}$$

Defining the solidity and drag/lift ratios as

$$\sigma = \frac{B \cdot C}{2 \cdot \pi \cdot r} \quad ; \quad \epsilon = \frac{C_D}{C_L}$$

the axial inflow factor is then determined by

$$\frac{a}{1 + a} = \frac{\sigma \cdot C_L}{4 \cdot \sin^2(\phi) \cdot F} \cdot (\cos(\phi) - \epsilon \cdot \sin(\phi)) \tag{3.7}$$

Similarly, the incremental torque as determined by momentum considerations must equate to that determined by blade element consideration.

$$dQ = 4\pi \cdot \rho \cdot r^3 \cdot \Omega \cdot V \cdot a' \cdot (1 + a) \cdot F \cdot dr = \frac{1}{2} \cdot B \cdot \rho \cdot W^2 \cdot C \cdot r \cdot (C_L \cdot \sin(\phi) + C_D \cdot \cos(\phi))$$

Noting also that:

$$W = V_{rel} = \frac{r \cdot \Omega \cdot (1 - a')}{\cos(\phi)}$$

$$V \cdot (1 + a) = r \cdot \Omega \cdot (1 - a') \cdot \tan(\phi)$$

$$\cos^2(\phi) \cdot \tan(\phi) = \sin(\phi) \cdot \cos(\phi)$$

the rotational inflow factor is determined by

$$\frac{a'}{1 - a'} = \frac{\sigma \cdot C_L}{4 \cdot \sin(\phi) \cdot \cos(\phi) \cdot F} \cdot (\sin(\phi) + \epsilon \cdot \cos(\phi)) \tag{3.8}$$

3.1.1 NACELLE INTERFERENCE

The governing equations as developed above require that the forward velocity, V, is radially constant along the propeller blades. To account for nacelle interference the equations must therefore be modified so as to accommodate a variable axial velocity component, u_x. This axial velocity is somewhat less than the corresponding free stream velocity, V, and is conveniently expressed as a ratio of the free stream velocity.

$$u = \frac{u_x}{V}$$

The mass flow rate through the propeller disc is then given by

$$\dot{dm} = V \cdot (u + a) \cdot \rho \cdot 2 \cdot \pi \cdot r \cdot dr$$

and as the inflow factor, v_1, is equal to one half of the incremental velocity, v_2, in the far wake, equation 3.3 can be rewritten in terms of the modified axial velocity, u.

$$dT = 4 \cdot \pi \cdot \rho \cdot r^2 \cdot V^2 \cdot a \cdot (u + a) \cdot F \cdot dr$$

Furthermore the axial inflow factor is determined by

$$\frac{a}{u + a} = \frac{\sigma \cdot C_L}{4 \cdot \sin^2(\phi) \cdot F} \cdot (\cos(\phi) - \epsilon \cdot \sin(\phi)) \quad \Rightarrow \textit{ solve for } a$$

The rotational inflow factor is insensitive to changes in the axial velocity and therefore need not be modified to include nacelle effects.

3.2 NUMERICAL SOLUTION

The solution to the analytical equations entails many computations at each blade element and several deeply nested iterative loops. Also the solution accuracy increases with the number of blade elements considered and with increasingly stringent convergence criterion. Therefore a numerical approach as outlined in steps 1 thru 13 below is necessary. Nacelle interference has been incorporated by means of the modified axial velocity, u. Note however that the nacelle constraint is removed by simply setting the variable, u, equal to one.

1) Specify initial values for the inflow factors.

   Relatively large values (a=15 a'=.5) are chosen as instabilities occur if the initial values are significantly lower than the actual values.

2) If nacelle interference is not considered then set the axial velocity factor, u, equal to one, $u(r)=u_x/V=1$.

   or

   If nacelle interference effects are to be considered then determine the modified axial velocity component as a function of the radius, $u(r)=u_x/V$.

3) Calculate ϕ, $W(=V_{rel})$, Mach No, and σ;

$$\phi = \tan^{-1}\left(\frac{V\cdot(1+a)}{r\cdot\Omega\cdot(1-a')}\right) \quad ; \quad a = \frac{v_1}{V} \quad ; \quad a' = \frac{\omega_1}{\Omega} \quad ; \quad u = \frac{u_x}{V}$$

$$W = \frac{V\cdot(1+a)}{\sin(\phi)}$$

$$Mach\ No = \frac{W}{SOS}$$

$$\sigma = \frac{B \cdot c}{2 \cdot \pi \cdot r}$$

4) Calculate angle of attack and determine lift/drag characteristic;

(N.B. lift curve slope can be modified as a function of Mach number)

$$\alpha = \beta - \phi \rightarrow C_L ; \frac{C_D}{C_L}$$

5) Calculate momentum loss factor (Prandtl)

$$F = \frac{2}{\pi} \cdot [\tan^{-1}(e^{2 \cdot f} - 1)]^{\frac{1}{2}}$$

$$f = \frac{B \cdot (1 - r/R)}{2 \cdot \sin(\phi_T)}$$

6) Determine Thrust and Torque factors;

$$T_e = C_L \cdot (\cos(\phi) - \varepsilon \cdot \sin(\phi))$$

$$Q_e = C_L \cdot (\sin(\phi) + \varepsilon \cdot \cos(\phi))$$

7) Re-calculate the inflow factors (a & a')

$$\frac{a}{u+a} = \frac{\sigma \cdot T_e}{4 \cdot F \cdot \sin^2(\phi)} \quad \Rightarrow \textit{ solve for a } \textit{(Gauss-Seidel iteration)}$$

$$\frac{a'}{1-a'} = \frac{\sigma \cdot Q_e}{4 \cdot F \cdot \sin(\phi) \cdot \cos(\phi)} \quad \Rightarrow \textit{ solve for a' } \textit{(Gauss-Seidel iteration)}$$

8) Repeat steps 3 thru 7 until the inflow factors converge

9) Calculate the thrust and torque derivatives

$$\frac{dT}{dr} = \frac{1}{2} \cdot B \cdot \rho \cdot W^2 \cdot C \cdot T_e$$

$$\frac{dQ}{dr} = \frac{1}{2} \cdot B \cdot \rho \cdot W^2 \cdot C \cdot r \cdot Q_e$$

10) Repeat steps 1 thru 9 for each blade element, beginning at the blade tip

11) Integrate over the entire blade radius

(Simpson's 1/3 and 3/8 rules):

$$THRUST = \int_{r_o}^{R} \frac{dT}{dr} \cdot dr \quad ; \quad TORQUE = \int_{r_o}^{R} \frac{dQ}{dr} \cdot dr$$

12) If the pitch is variable and the calculated required power is not equal to the engine power at the specified RPM, then adjust the pitch and repeat steps 1 thru 10 until the calculated power and engine power converge.

or

If the engine RPM is variable and the calculated required power is not equal to the engine power at the particular RPM, then adjust the RPM and repeat steps 1 thru 10 until the calculated power and engine power converge.

13) Calculate performance parameters:

$$C_T = \frac{Thrust}{\rho \cdot \Omega^2 \cdot D^4}$$

$$C_P = \frac{Power}{\rho \cdot \Omega^3 \cdot D^5}$$

$$\eta = \frac{THRUST * V}{POWER}$$

3.2.1 CONVERGENCE CRITERION

Within the analysis routine, a Gauss-Seidel iterative technique has been utilized to determine the axial and rotational inflow factors. The main advantage of Gauss-Seidel is that the relaxation factor can be manipulated to minimize numerical instability. That is, when large gradients are encountered the relaxation factor can be made very small. It has been found that relaxation factors as small as 0.025 are necessary to prevent instabilities near the blade tips at some off design conditions. The relaxation factors could be arbitrarily set at a very low value but this may unnecessarily increase the computing time. Therefore the relaxation factors, W_1 and W_2, should be set at the largest possible value which just inhibits instability. Also, a tolerance level of 0.0001 has been utilized and found to be sufficient;

$$\textit{when} \quad |(a - a_{-1})| > 0.0001 \quad \Rightarrow \quad a = a + W_1 * (a_{-1} - a)$$

$$\textit{when} \quad |(a' - a'_{-1})| > 0.0001 \quad \Rightarrow \quad a' = a' + W_2 * (a'_{-1} - a')$$

It is often difficult to converge onto a solution at sections near the blade tip as the momentum loss factor, F, has a very large gradient and actually approaches zero. The instability can be minimized by substantially reducing the relaxation factor, but in some instances such as a propeller with square tipped blades a solution may not be possible at all. For a square blade tip at which F approaches zero, σ, C_L, and ϕ are finite, which result in mathematical inconsistencies of the expression:

$$\frac{a}{1+a} = \frac{\sigma \cdot C_L}{4 \cdot F \cdot \sin^2(\phi)} \cdot (\cos(\phi) - \epsilon \cdot \sin(\phi))$$

It has been suggested [22,23,24] that in this circumstance the axial inflow factor, a, should be clipped at -0.5 and the rotational inflow factor, a', at 0.7. The author however has suggested an alternative to this approach of simply limiting the values to which the solution diverges. It is reasonable to assume that the induced velocity in the far wake is in fact finite at the blade tip radius and actually approaches zero at a point just greater

than the tip radius. A relatively small distance equal to 1/100th of the blade diameter has been utilized herein, and found to be sufficient. The velocity distribution in the far wake is then shifted slightly and Prandtl's momentum loss factor F becomes

$$F = \frac{2}{\pi} \cdot \cos^{-1}(e^{-f})$$

$$f = \frac{B(1 + .005 - r/R)}{2 \cdot \sin(\phi_T)}$$

Also it has been found that to eliminate instability, the initial estimates for the inflow coefficients must be slightly larger than the actual values. Arbitrarily large initial estimates of 15 for the axial inflow coefficient and .5 for the rotation inflow coefficient are found to be adequate for most lightly loaded propellers. Furthermore in an effort to decrease the number of iterations, the initial inflow velocities are taken as the inflow factors determined at the previous blade section. If however these initial inflow factors are negative or excessively large, the solution has a tendency to diverge. Therefore a check statement must be written into the routine such that if the initial axial and rotational inflow velocities are negative or excessive, they are automatically reset to 15 and 0.5 respectively.

The simplifying assumption of a helicoidal trailing vortex wake at all operating conditions further inhibits convergence. The helicoidal wake is correct for analysis at the design conditions but at off design conditions the wake becomes somewhat distorted and coincides with a slightly modified induced velocity distribution. As a result of the inaccurate wake model at far off design conditions, convergence is often difficult and therefore the tolerance levels are necessarily increased.

3.2.2 FIXED PITCH

In considering a particular propeller-engine configuration, both the aerodynamic characteristics of the propeller and the performance characteristics of the engine are required. For the fixed pitch configuration the engine RPM will vary until the engine power exactly matches the power required by the propeller. That is, an entire analysis of the blade is carried out at a particular RPM and if the calculated power is not within one percent of the engine power the RPM is changed and the analysis carried out again. A Newton-Raphson iterative technique with relaxation has been utilized in this instance as it converges onto the correct RPM very quickly.

$$when \quad |(HP_{prop} - HP_{engine})| > .01 * HP_{engine}$$

$$\Rightarrow \quad RPM_{i+1} = RPM_i - \frac{f(RPM_i)}{f'(RPM_i)}$$

$$where, \quad f(RPM_i) = HP_{prop} - HP_{engine}$$

$$f'(RPM_i) \approx \frac{f(RPM_i) - f(RPM_{i-1})}{RPM_i - RPM_{i-1}}$$

The accuracy of the fixed pitch analysis routine depends largely upon the accuracy of the element airfoil characteristics. Under ideal operating conditions the airflow around each blade section remains fully attached. The lift and drag characteristics corresponding to the blade geometry are then fully representative and an accurate analysis can be carried out. When the operating conditions are not ideal as for example at excessive forward speeds or at static conditions, some blade sections begin to stall. That is, the flow around the blade sections separates resulting in a loss of lift and a significant increase in drag. Unfortunately aerodynamic stall characteristics are very difficult to predict analytically and little experimental data is available. Therefore the approach taken here has been to accurately determine the aerodynamic coefficients at all angles of attack corresponding to fully attached flow, and approximate the aerodynamic coefficients corresponding to separated flow (stall).

3.2.2.1 APPROXIMATE AERODYNAMIC STALL CHARACTERISTICS

The lift/drag characteristics corresponding to the fully attached flows are shown generally by the dotted lines in Figure 19. As proposed by E.E. Larabee [25] the post-stall lift and drag coefficients represented by the solid lines in Figure 19, are approximated with cosine and sine functions respectively.

$$CL = \frac{CL_1}{\cos(\alpha_1)}\cos(\alpha) \qquad (\alpha \le \alpha_1)$$

$$CL = \frac{CL_2}{\cos(\alpha_2)}\cos(\alpha) \qquad (\alpha \ge \alpha_2)$$

$$CD = |\sin(\alpha)| \qquad (\alpha_1 \ge \alpha \ge \alpha_2)$$

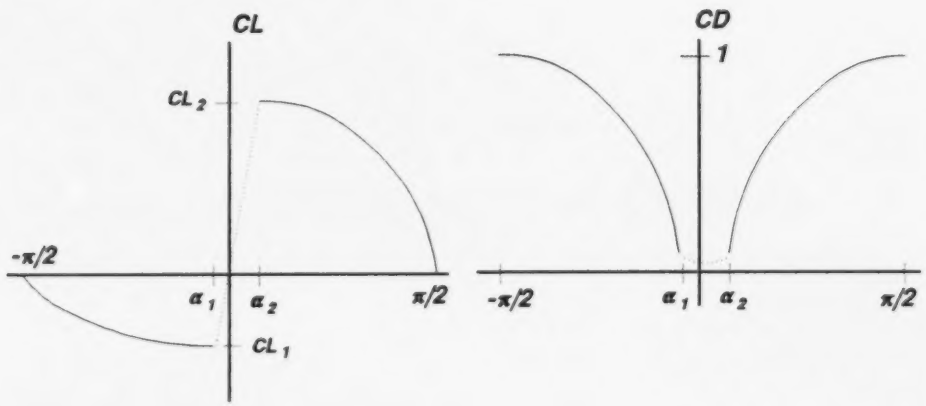

Figure 19, Airfoil Stall Characteristics

3.2.3 VARIABLE PITCH

The variable pitch or constant speed propeller provides high propulsive efficiency over a wide operating range. This configuration not only has a higher efficiency over a wider range than the fixed pitch configuration but the corresponding analysis routine is generally more accurate. A marginal increase in accuracy can be attributed to the fact that only one point on the engine performance is required as opposed to the entire engine characteristic curve. Therefore any errors introduced by uncertainties in the engine characteristics are significantly minimized. A further increase in accuracy results from the fact that the propeller pitch is adjusted such that blade stall is minimized. Fewer stall characteristics are required and hence fewer errors are introduced by uncertainties in the stall characteristic data.

A Newton-Raphson iterative routine similar to that used for the fixed pitch analysis is utilized. At the specified engine RPM and power a full analysis of the propeller is carried out. If the calculated power is not equal to the engine power, the geometric mean pitch [26] is adjusted and the analysis carried out again. This process is continued until the calculated power comes to within one percent of the specified power.

$$when \quad |(HP_{prop} - HP_{engine})| > .01 * HP_{engine}$$

$$\Rightarrow \quad Pitch_{i+1} = Pitch_i - \frac{f(Pitch_i)}{f'(Pitch_i)}$$

$$where, \quad f(Pitch_i) = HP_{prop} - HP_{engine}$$

$$f'(Pitch_i) \approx \frac{f(Pitch_i) - f(Pitch_{i-1})}{Pitch_i - Pitch_{i-1}}$$

3.3 VERIFICATION

As the analysis routine is based on theoretical principles and utilizes various numerical techniques it is necessary to verify the results experimentally. For this purpose a light aircraft with a three bladed fixed pitch propeller powered with a Rotax 532 engine was made available.

Manufacturers specifications were not available for the propeller so several measurements of the propeller geometry were taken and are shown in Table 3.

Table 3, Propeller Geometry

3 Blades ; Prop Diameter = 64 in ; Hub Diameter = 14 in Geometric Mean Pitch** = 52.3 in Nacelle Diameter ≈ 32 in @ firewall			
Radius (in)	Chord (in)	* β (degs)	** β (degs)
7	5.0	23.03	28.53
11	4.7	20.31	25.61
15	4.2	17.92	22.92
19	3.7	15.98	20.98
23	3.2	14.43	19.43
27	2.8	13.38	18.38
31	2.2	12.56	17.56

* w.r.t. bottom of blade

** w.r.t. zero lift line

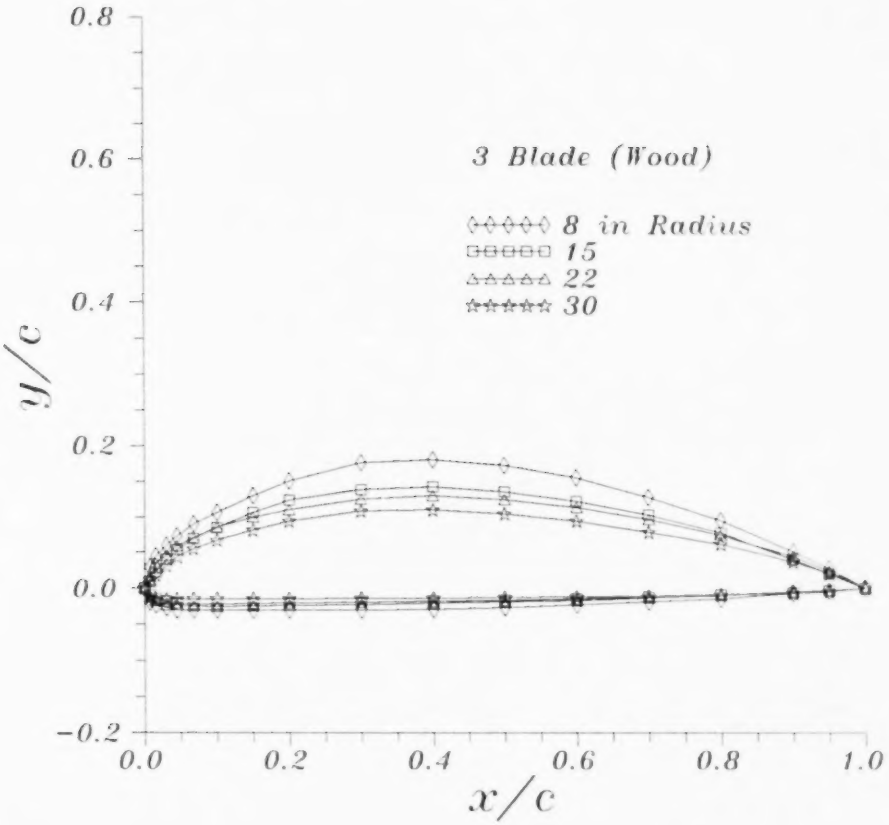

Figure 20, Blade Airfoil Coordinates for Test Propeller

Also as the blade airfoil characteristics were not known, the airfoil coordinates were measured at blade radii of 8, 15, 22, 30 inches. As shown in Figure 20 the airfoil sections are relatively thick near the blade root and become thinner towards the blade tip. These four airfoil sections were analyzed with an airfoil analysis program developed by Kennedy & Marsden [27,28], which predicted the lift and drag characteristics shown in Figure 21. The stall characteristics were approximated with appropriate sine and cosine functions.

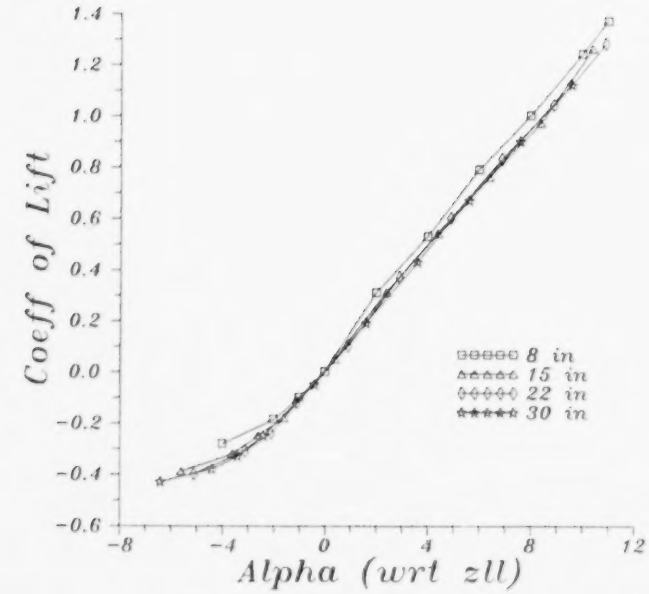

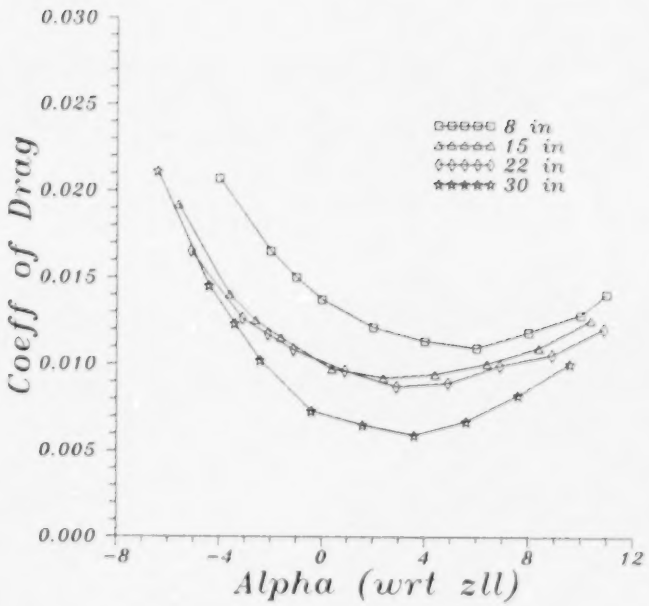

Figure 21, Lift and Drag Curves for Test Propeller

The performance characteristics of the Rotax 532 engine at sea level are specified by the manufacturer and are shown in Figure 22. An engine gear reduction ratio of 2.58:1 was utilized and an appropriate correction for the engine power was introduced to account for altitude and temperature changes.

$$HP = HP_{rated} / \left(1.18\frac{\sqrt{T_R}}{P_R} - .18\right)$$

$$where\ ,\quad T_R = \frac{Temp(\circ C) + 273.15}{288}$$

$$P_R = \left(1 - 6.89\frac{Alt}{10^6}\right)^{5.256}$$

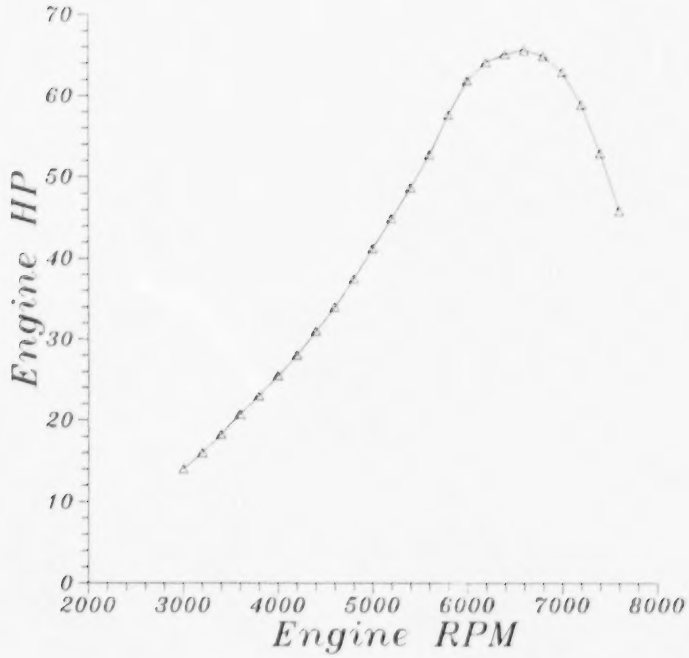

Figure 22, Rotax 532 Performance Curve

Having determined the propeller geometry, blade aerodynamic characteristics, and engine characteristics the theoretical propeller performance curves were calculated using the analysis routine. The minimum forward velocity considered was 20 knots because at slower velocities the blades were fully stalled. The analysis routine still converges if small relaxation factors are utilized but the results are unrepresentative because of uncertainties in the aerodynamic stall data. Theoretical curves calculated at 3000 feet above sea level, 15 degrees celcius, and at a geometric mean pitch of 52.3 inches are plotted as a function of forward velocity in Figures 23 thru 29. All the curves indicate trends typical of fixed pitch propellers but of particular interest is the engine RPM as it can be compared directly with experimental measurements. The engine RPM was measured experimentally at several flight speeds and is compared against the theoretical values in Table 4.

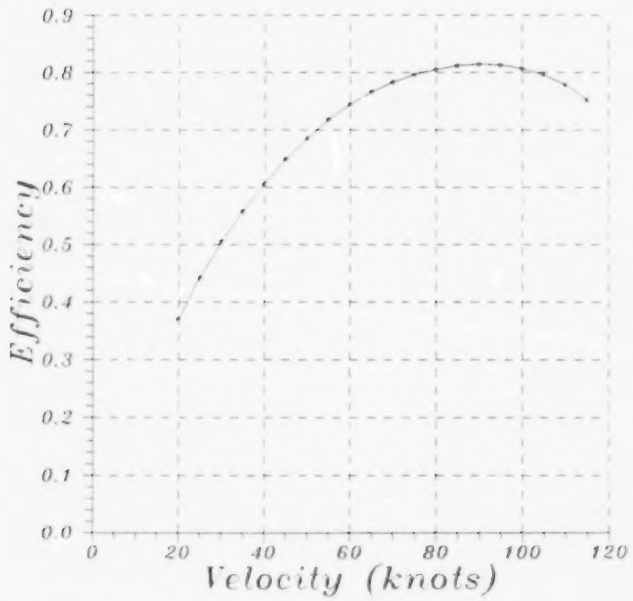

Figure 23, Efficiency vs. Forward Velocity

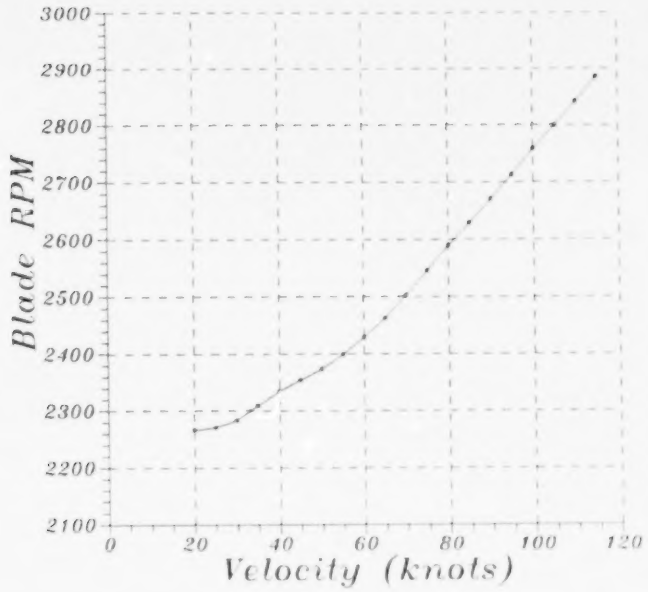

Figure 24, Blade RPM vs. Forward Velocity

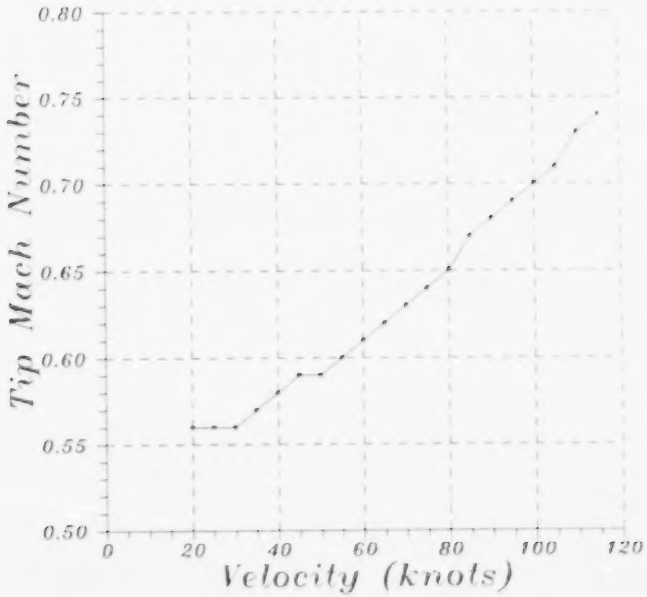

Figure 25, Tip Mach Number vs. Forward Velocity

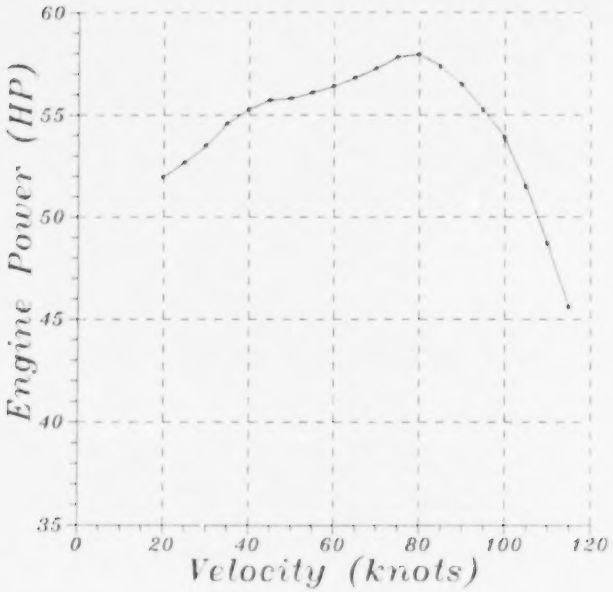

Figure 26, Engine Power vs. Forward Velocity

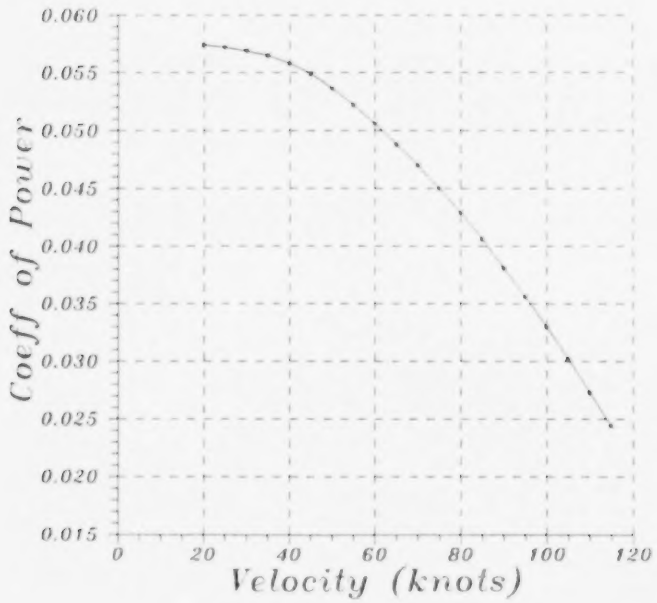

Figure 27, Coefficient of Power vs. Forward Velocity

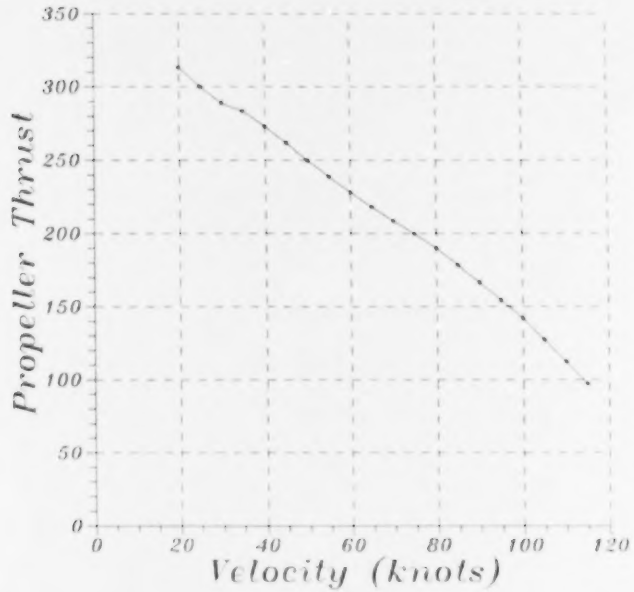

Figure 28, Propeller Thrust vs. Forward Velocity

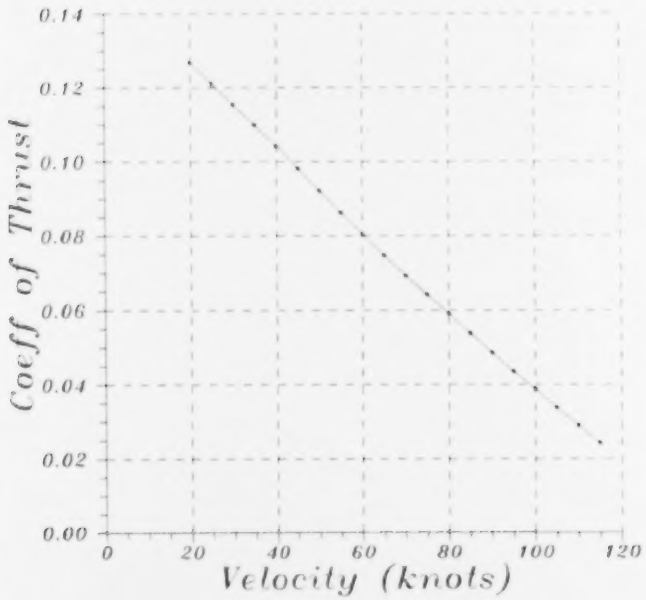

Figure 29, Coefficient of Thrust vs. Forward Velocity

Table 4, Measured vs. Calculated Engine RPM for Test Propeller

* *Forward Velocity*		*Engine RPM*			** *Vortex Sheet Spacing*
M.P.H.	*Knots*	*Measured*	*+ Analysis*	*^ %Error*	
0	0	6200	----	----	0
31.4	27.3	6100	6073	0.4	.146
41.8	36.3	6500	6120	5.8	.193
52.3	45.4	6600	6201	6.0	.238
68.0	54.5	6750	6322	6.3	.279
83.6	72.7	7000	6643	5.1	.352
94.1	81.8	7200	6820	5.3	.385

* True Air Speed - (Correction Factor = 1.0454 @ 3000 ft & 15 °C)

\+ Stall characteristics approximated with sine and cosine functions
Geometric Mean Pitch = 52.3"
Itt Tol = 0.5 HP ; Rlx Fctrs = .1

^ %Error = (Measured RPM - Analytical RPM) / Measured RPM

** Based on geometrical mean pitch of 52.3" and analytical RPM

$$\frac{b}{R} = \frac{2\pi}{B}\frac{\lambda}{\sqrt{\lambda^2+1}} \qquad \textit{where, } \lambda = \frac{V}{\Omega \cdot R} = \frac{J}{\pi}$$

As shown in Table 4 the theoretical RPM corresponding to the measured blade pitch was slightly less than the measured RPM for all the forward velocities considered. The largest difference between the measured and analytical RPM was 6.3% at 54.5 knots. A 6.3% error is acceptable but it is worthy to note that this error would likely decrease if the pitch and aerodynamic characteristics were determined more accurately.

From Table 4 it is also seen that the vortex sheet spacing is much less than the propeller radius. As a result Prandtl's approximation to Goldstein's exact solution is itself almost exact. The assumption of a rigid helicoidal wake enables Prandtl's momentum loss factor to be implemented into the momentum equations and therefore increase the accuracy of the analysis routine. However as the wake is actually only helicoidal near the design condition, Prandtl's momentum loss factor may not be correct over the entire operating range. To assess the sensitivity of analytical results to Prandtl's momentum loss factor determined for a helicoidal wake, two velocity distributions have been considered. Prandtl's velocity distribution was shifted radially outwards by factors of 0.005 and 0.2, which correspond generally to $F \neq \text{const}$ and $F = \text{const}$ in Figure 30.

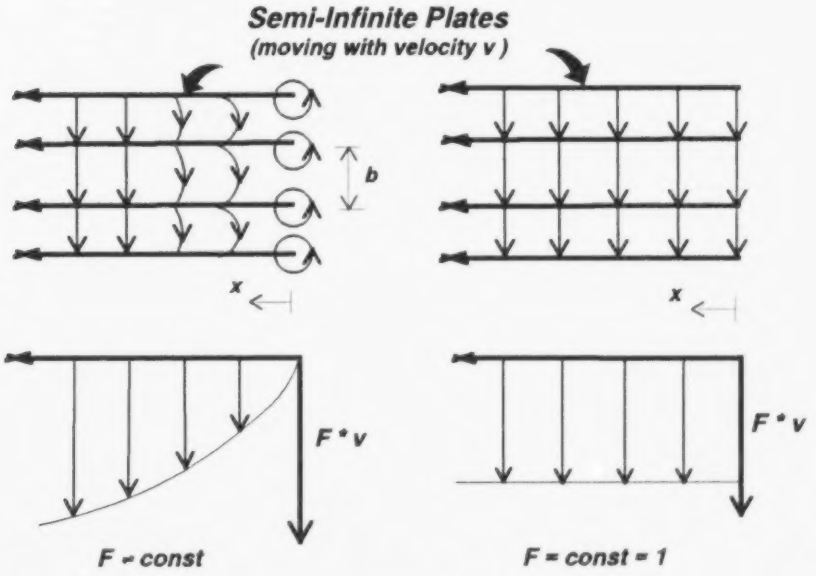

Figure 30, Prandtl's Distribution Modified

It is seen from Table 5 that the discrepancies between the measured and analytical RPM's for the two cases increase with velocity. This trend is attributable to the fact that as the forward velocity increases the spacing between the vortex sheets also increases and consequently more of the blade if subject to Prandtl's momentum losses. With more of the blade subject to Prandtl's momentum loss factors the analysis routine then becomes more sensitive to shifts of Prandtl's distribution. For the velocity range considered here Prandtl's momentum losses are practically insignificant, but nevertheless the inclusion of Prandtl's momentum losses did improve the accuracy.

Table 5, Engine RPM as Calculated for 3 Modified Prandtl Distributions

* *Forward Velocity*		*Engine RPM*			
M.P.H.	*Knots*	*Measured*	*+ Analysis*	*^ Analysis*	*~ Anal Diff*
0	0	6200	----	----	----
31.4	27.3	6100	6073	6049	24
41.8	36.3	6500	6120	6073	47
52.3	45.4	6600	6201	6137	64
68.0	54.5	6750	6322	6252	70
83.6	72.7	7000	6643	6559	84
94.1	81.8	7200	6820	6726	94

* True Air Speed - (Correction Factor = 1.0454 @ 3000 ft)

+ Prandtl's distribution shifted by 0.005

^ Prandtl's distribution shifted by 0.2 (Uniform)

~ $RPM_{(.005\ shift)} - RPM_{(.2\ shift)}$

Geometric Mean Pitch = 52.3" ; Itt Tol = 0.5 HP ; Rlx Fctrs = 0.1

Chapter 4

Design

4.0 DESIGN

The design methodology developed herein is based upon classical theory and in particular, Betz's optimum wake. The propeller blades are designed so as to produce a helicoidal trailing vortex wake with a constant displacement velocity.

4.1 DERIVATION OF GOVERNING EQUATIONS

The basic approach taken in propeller design is similar to that used for analysis. That is, the governing equations are also assessed at each blade element and then integrated over the entire blade. Applying the conservation of momentum and continuity across the propeller flow field, a set of expressions for the thrust and torque at each blade element is obtained. An additional set of equations is obtained by considering the classical blade element theory. These two sets of equations for the elemental torque and thrust are then equated and relations for the corresponding inflow velocities are obtained.

The first set of equations for the elemental thrust and torque are derived from the conservation of momentum. From conservation of linear momentum the thrust is

$$dT = \dot{dm} \cdot v_2 \cdot F \tag{4.1}$$

and similarly by conservation of angular momentum the torque is

$$dQ = r \cdot \dot{dm} \cdot (r \cdot \omega_2) \cdot F \tag{4.2}$$

Prandtl's momentum loss factor, F, establishes the induced velocity distribution corresponding to a helicoidal trailing vortex wake and is approximated by

$$F = \frac{2}{\pi} \cdot \cos^{-1}(e^{-f})$$

$$f = \frac{B \cdot (1 - r/R)}{2 \cdot \sin(\phi_T)} \qquad \textit{where, } \phi_T = \phi \textit{ at blade tip}$$

The incremental velocities v_2 and ω_2 taken in the far wake are represented in terms of the inflow factors a and a' by;

$$a = \frac{v_1}{V} \; ; \quad v_1 = \frac{1}{2} v_2 \qquad \Rightarrow v_2 = 2aV$$

$$a' = \frac{\omega_1}{\Omega} \; ; \quad \omega_1 = \frac{1}{2} \omega_2 \qquad \Rightarrow \omega_2 = 2a'\Omega$$

and the mass flow rate calculated at the propeller disc is given by

$$\dot{dm} = V \cdot (1 + a) \cdot \rho \cdot 2 \cdot \pi \cdot r \cdot dr$$

Equations 4.1 and 4.2 can then be rewritten as

$$dT = 4 \cdot \pi \cdot \rho \cdot r \cdot V^2 \cdot a \cdot (1 + a) \cdot F \cdot dr \tag{4.3}$$

$$dQ = 4 \cdot \pi \cdot \rho \cdot r^3 \cdot \Omega \cdot V \cdot (1 + a) \cdot a' \cdot F \cdot dr \tag{4.4}$$

The additional set of equations for the incremental thrust and torque is arrived at through aerodynamic blade element considerations which again is analogous to the approach taken in the analysis section. However, rather than determining the element forces in terms of lift and drag coefficients, the forces are represented in terms of the element circulation, Γ. Finite airfoil theory shows that the lift per unit radius on a blade element can be expressed in terms of the air density, relative velocity, and circulation by

$$L' = B \cdot \rho \cdot W \cdot \Gamma$$

As shown in Figure 31 the lift per unit radius, L', and viscous drag per unit radius, D', are split into axial and rotational components representing the thrust and torque respectively.

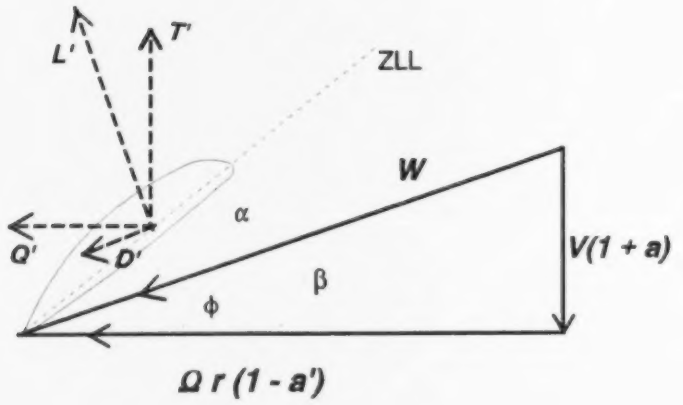

Figure 31, Blade Element Theory

The elemental thrust and torque components are then given by

$$\frac{dT}{dr} = T' = L'\cdot\cos(\phi) - D'\cdot\sin(\phi)$$

$$= L'\cdot\cos(\phi)\cdot(1 - \epsilon\cdot\tan(\phi)) \tag{4.5}$$

$$\frac{dQ}{dr} = Q' = [L'\cdot\sin(\phi) + D'\cdot\cos(\phi)]\cdot r$$

$$= [L'\cdot\sin(\phi)\cdot(1 + \frac{\epsilon}{\tan(\phi)})]\cdot r \tag{4.6}$$

$$\textit{where,} \quad \phi = \tan^{-1}(\frac{V\cdot(1+a)}{r\cdot\Omega\cdot(1-a')})$$

$$\epsilon = \frac{D'}{L'}$$

In equations 4.5 and 4.6 above, the drag component need not be evaluated because it has been expressed as a function of the lift by means of the D'/L' ratio. However as the lift component must still be evaluated an expression for the element circulation, Γ, corresponding to the optimum wake must be derived. Vortex theory shows that the circulation about the propeller blades can be equated to the circulation in the propeller slipstream. In terms of the slipstream tangential velocity

$$w_t = v' \cdot \cos(\phi) \cdot \sin(\phi) \cdot F$$

the blade circulation is given by

$$B \cdot \Gamma = v' \cdot \cos(\phi) \cdot \sin(\phi) \cdot F \cdot 2 \cdot \pi \cdot r \tag{4.7}$$

Furthermore by introducing the displacement velocity factor, ζ

$$\zeta = \frac{v'}{V}$$

and the circulation function, G

$$G = F \cdot X \cdot \cos(\phi) \cdot \sin(\phi) \qquad \textit{where,} \quad X = \frac{\Omega \cdot r}{V}$$

the total blade circulation in equation 4.7 can be rewritten as

$$\Gamma = \frac{2 \cdot \pi \cdot V^2 \cdot \zeta \cdot G}{B \cdot \Omega}$$

The lift per unit radius expressed in terms of the element circulation is then

$$L' = B \cdot \rho \cdot W \cdot \Gamma$$

$$= B \cdot \rho \cdot W \cdot \left(\frac{2 \cdot \pi \cdot V^2 \cdot \zeta \cdot G}{B \cdot \Omega}\right) \tag{4.8}$$

Also from the above expression for lift, L', the blade chord can be determined as by

$$c = \frac{4 \cdot \pi \cdot V^2 \cdot G \cdot \zeta}{C_L \cdot W \cdot \Omega \cdot B} \qquad where, \quad C_L = \frac{L'}{\frac{1}{2} \cdot \rho \cdot W^2 \cdot c}$$

The incremental thrust as determined by both momentum and blade element considerations can now be manipulated to assess the inflow velocities. Equations 4.3 and 4.5 representing the incremental thrust, are equivalent and can be equated with one another.

$$dT = 4 \cdot \pi \cdot \rho \cdot r \cdot V^2 \cdot a \cdot (1 + a) \cdot F \cdot dr = L' \cdot \cos(\phi) \cdot (1 - \epsilon \cdot \tan(\phi)) \cdot dr$$

The lift per unit radius, L', is expressed in terms of the circulation, Γ, by equation 4.8

$$2 \cdot r \cdot a \cdot (1 + a) \cdot F = \frac{W \cdot \zeta \cdot G \cdot \cos(\phi) \cdot (1 - \epsilon \cdot \tan(\phi)}{\Omega}$$

and the circulation function, G, can be expanded such that

$$2 \cdot a \cdot (1 + a) = \frac{W \cdot \zeta \cdot \sin(\phi) \cdot \cos^2(\phi) \cdot (1 - \epsilon \cdot \tan(\phi))}{V}$$

Furthermore, taking note of the velocity vectors in Figure 31

$$V \cdot (1 + a) = W \cdot \sin(\phi)$$

the axial inflow factor is given by

$$a = (\frac{\zeta}{2}) \cdot \cos^2(\phi) \cdot (1 - \epsilon \cdot \tan(\phi)) \tag{4.9}$$

Similarly the incremental torque as determined by both momentum and blade element considerations can be manipulated to assess the rotational inflow velocities. The incremental torque given by equations 4.4 and 4.6 are equated with one another

$$dQ = 4 \cdot \pi \cdot \rho \cdot r^3 \cdot \Omega \cdot V \cdot (1 + a) \cdot a' \cdot F \cdot dr = L' \cdot \sin(\phi) \cdot (1 + \frac{\epsilon}{\tan(\phi)}) \cdot r \cdot dr$$

The lift per unit radius, L', is again expressed in terms of the circulation, Γ

$$4\cdot\pi\cdot\rho\cdot r^3\cdot\Omega\cdot V\cdot(1+a)\cdot a'\cdot F\cdot dr = B\cdot\rho\cdot W\cdot\sin(\phi)\left(\frac{2\cdot\pi\cdot V^2\cdot\zeta\cdot G}{B\cdot\Omega}\right)\left(1+\frac{\epsilon}{\tan(\phi)}\right)r\cdot dr$$

and the circulation function, G, is expanded such that

$$2\cdot r\cdot\Omega\cdot(1+a)\cdot a' = W\cdot\zeta\cdot\cos(\phi)\cdot\sin^2(\phi)\cdot\left(1+\frac{\epsilon}{\tan(\phi)}\right)$$

Also taking note of the velocity vectors in Figure 31

$$V\cdot(1+a) = W\cdot\sin(\phi) \qquad ; \quad X = \frac{\Omega\cdot r}{V}$$

the rotational inflow factor is given by

$$a' = \left(\frac{\zeta}{2\cdot X}\right)\cdot\cos(\phi)\cdot\sin(\phi)\cdot\left(1+\frac{\epsilon}{\tan(\phi)}\right) \tag{4.10}$$

In the above expressions for the axial and inflow factors, the angle, ϕ, must be assessed and is most illustrative when determined for a frictionless blade. Therefore ignoring friction the axial and rotational inflow factors reduce to

$$a = \left(\frac{\zeta}{2}\right)\cdot\cos^2(\phi) = \frac{v'}{2\cdot V}\cdot\cos^2(\phi)$$

$$\Rightarrow \quad a\cdot V = \frac{v'}{2}\cdot\cos^2(\phi)$$

$$a' = \left(\frac{\zeta}{2\cdot X}\right)\cdot\cos(\phi)\cdot\sin(\phi) = \frac{v'}{2\cdot\Omega\cdot r}\cdot\cos(\phi)\cdot\sin(\phi)$$

$$\Rightarrow \quad a'\cdot\Omega\cdot r = \frac{v'}{2}\cdot\cos(\phi)\cdot\sin(\phi)$$

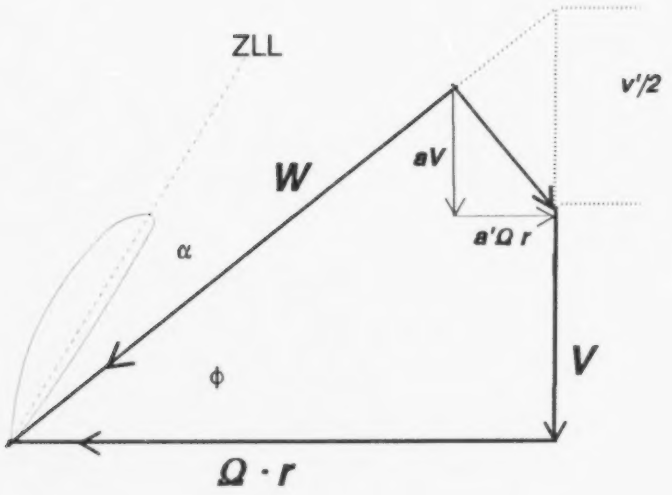

Figure 32, Vector Diagram of Design Induced Velocities

As shown in Figure 32, these expressions are satisfied if the total induced velocity acts at right angles to the resultant velocity, W. Also, as confirmed by actuator disc and momentum theory, the displacement velocity at the propeller is in fact equal to v'/2. The angle of attack is thus determined by

$$\phi = \tan^{-1}\left(\frac{V + v'/2}{\Omega \cdot r}\right)$$

$$= \tan^{-1}\left[\left(1 + \frac{\zeta}{2}\right)/X\right]$$

Alternatively by introducing the advance ratio, λ, and dimensionless radius, ξ

$$\lambda = \frac{V}{\Omega \cdot R} \quad ; \quad \xi = \frac{r}{R}$$

the angle ϕ can be rewritten as

$$\phi = \tan^{-1}\left[\left(1 + \frac{\zeta}{2}\right) \cdot \frac{\lambda}{\xi}\right] \tag{4.11}$$

Equation 4.11 above is very simple and is therefore easily incorporated into a design routine. However as the design routine takes viscous drag into account the expression for ϕ must be reassessed in terms of viscous drag. Again considering equations 4.9 and 4.10 it is seen that viscous drag reduces the axial inflow velocity, v_1, by $aV\epsilon\tan(\phi)$ and increases the rotational inflow velocity, ω_1, by $a'\Omega r\epsilon/\tan(\phi)$. Thus as shown in Figure 33, the relative velocity, W, is reduced and the induced velocity vector, w_{ii}, becomes representative of a flow with viscous drag. Furthermore it is seen that the angle ϕ' calculated in terms of the change in axial and rotational inflow velocities due to the introduction of viscous drag is in fact equal to the angle ϕ.

$$\tan(\phi') = \frac{a \cdot V \cdot \epsilon \cdot \tan(\phi)}{a' \cdot \Omega \cdot r \cdot \epsilon / \tan(\phi)} = \tan(\phi)$$

$$\textit{where,} \quad \tan(\phi) = \frac{a' \cdot \Omega \cdot r}{a \cdot V}$$

Therefore the resultant velocity, W, acts at the same angle, ϕ, as that for frictionless flow and equation 4.11 is valid when viscous drag is introduced into the design.

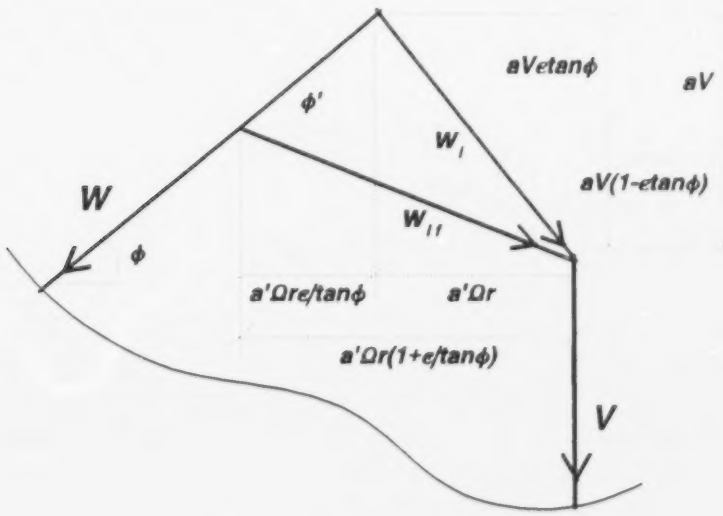

Figure 33, Effect of Friction on Optimum Design Condition

4.1.1 CONSTRAINTS

The design routine developed herein determines the optimum blade geometry for a given set of design conditions. These design conditions consist of parameters such as the propeller radius, hub radius, airfoil characteristics, forward velocity, and engine characteristics. The most significant design requirement however, is the developed thrust or required power, as when represented in terms of corresponding non-dimensional coefficients they can be effectively utilized as constraints in the iterative design routine. It is then necessary to express the thrust and power coefficients in terms of the design variables.

Noting that the angle, ϕ, lift component, L', and circulation, Γ, are given by

$$\cos(\phi) = \frac{\Omega \cdot r \cdot (1 - a')}{W} \quad ; \quad L' = B \cdot \rho \cdot W \cdot \Gamma \quad ; \quad \Gamma = \frac{2 \cdot \pi \cdot V^2 \cdot \zeta \cdot G}{B \cdot \Omega}$$

the thrust component as given by blade element considerations

$$T' = L' \cdot \cos(\phi) \cdot (1 - \epsilon \cdot \tan(\phi))$$

can be expanded and then reduced to the more explicit form

$$T' = 2 \cdot \pi \cdot \rho \cdot V^2 \cdot \zeta \cdot G \cdot r \cdot (1 - a') \cdot (1 - \epsilon \cdot \tan(\phi)) \tag{4.12}$$

Furthermore by substituting equation 4.10 for the rotational inflow factor, a', into equation 4.12, the thrust, T', can be expressed as a function of ς and ς^2.

$$T' = 2 \cdot \pi \cdot \rho \cdot V^2 \cdot G \cdot r \cdot (1 - \epsilon \cdot \tan(\phi)) \cdot [\zeta - \frac{V \cdot \cos(\phi) \cdot \sin(\phi)}{2 \cdot \Omega \cdot r} \cdot (1 + \frac{\epsilon}{\tan(\phi)}) \cdot \zeta^2]$$

Now as the thrust depicted in the non-dimensional thrust coefficient

$$T_c = \frac{2 \cdot T}{\rho \cdot V^2 \cdot \pi \cdot R^2}$$

is not specified per unit radius, its derivative must be determined by differentiation of the thrust coefficient. Following Larabee [18] and Adkins [22], the thrust coefficient as

differentiated with respect to the non-dimensional radius, ξ, is

$$T_c' = \frac{dT_c}{d\xi} = \frac{dT}{dr}\cdot\frac{dr}{d\xi}\cdot\left(\frac{2}{\rho\cdot V^2\cdot\pi\cdot R^2}\right)$$

$$= T'\cdot\left(\frac{2}{\rho\cdot V^2\cdot\pi\cdot R}\right)$$

Introducing the derivatives I_1' and I_2', taken with respect to the dimensionless radius, ξ

$$I_1' = \frac{dI_1}{d\xi} = 4\cdot\xi\cdot G\cdot(1-\epsilon\cdot\tan(\phi))$$

$$I_2' = \frac{dI_2}{d\xi} = \lambda\cdot\left(\frac{I_1'}{2\cdot\xi}\right)\cdot\left(1+\frac{\epsilon}{\tan(\phi)}\right)\cdot\sin(\phi)\cdot\cos(\phi)$$

the thrust coefficient per unit radius is given by

$$T_c' = I_1'\cdot\zeta - I_2'\cdot\zeta^2 \qquad (4.13)$$

Analogous to the above derivation the power can be represented in terms of the non-dimensional power coefficient. Again noting that the angle, ϕ, the lift component, L', and the circulation, Γ, are given by

$$\sin(\phi) = \frac{V\cdot(1+a)}{W} \quad ; \quad L' = B\cdot\rho\cdot W\cdot\Gamma \quad ; \quad \Gamma = \frac{2\cdot\pi\cdot V^2\cdot\zeta\cdot G}{B\cdot\Omega}$$

the torque component as given by blade element considerations

$$Q' = [L'\cdot\sin(\phi)\cdot(1+\frac{\epsilon}{\tan(\phi)})]\cdot r$$

can also be expanded and then reduced to the more explicit form

$$Q' = \frac{2\cdot\pi\cdot r\cdot\rho\cdot V^3\cdot G\cdot\zeta}{\Omega}\cdot(1+a)\cdot\left(1+\frac{\epsilon}{\tan(\phi)}\right) \qquad (4.14)$$

Substituting equation 4.9 for the axial inflow factor, a, into equation 4.14, the torque, Q', can be expressed as a function of ς and ς^2.

$$Q' = \frac{2 \cdot \pi \cdot r \cdot \rho \cdot V^3 \cdot G}{\Omega} \cdot (1 + \frac{\epsilon}{\tan(\phi)}) \cdot [\zeta + \frac{1}{2} \cdot \cos^2(\phi) \cdot (1 - \epsilon \cdot \tan(\phi)) \cdot \zeta^2]$$

Now as the torque depicted in the non-dimensional power coefficient

$$P_c = \frac{2 \cdot P}{\rho \cdot V^3 \cdot \pi \cdot R^2} = \frac{2 \cdot Q \cdot \Omega}{\rho \cdot V^3 \cdot \pi \cdot R^2}$$

is not specified per unit radius, its derivative must also be determined by differentiation of the power coefficient. Again following Larabee and Adkins [18,22], the power coefficient as differentiated with respect to the non-dimensional radius, ξ, is

$$P_c' = \frac{dP_c}{d\xi} = \frac{dQ}{dr} \cdot \frac{dr}{d\xi} \cdot (\frac{2 \cdot \Omega}{\rho \cdot V^3 \cdot \pi \cdot R^2})$$

$$= Q' \cdot (\frac{2 \cdot \Omega}{\rho \cdot V^3 \cdot \pi \cdot R})$$

Introducing the derivatives J_1' and J_2', taken with respect to the dimensionless radius, ξ

$$J_1' = \frac{dJ_1}{d\xi} = 4 \cdot \xi \cdot G \cdot (1 + \frac{\epsilon}{\tan(\phi)})$$

$$J_2' = \frac{dJ_2}{d\xi} = \frac{J_1'}{2} \cdot \cos^2(\phi) \cdot (1 - \epsilon \cdot \tan(\phi))$$

the power coefficient per unit radius is given by

$$P_c' = J_1' \cdot \zeta + J_2' \cdot \zeta^2 \qquad (4.15)$$

Either the thrust developed or power required must be specified in the design. If the thrust is specified the derivatives, I_1' and I_2', are evaluated from $\xi=\xi_0$ to $\xi=1$ and ζ is taken as the positive root of equation 4.13.

$$\zeta = \frac{I_1}{2 \cdot I_2} - [(\frac{I_1}{2 \cdot I_2})^2 - \frac{T_c}{I_2}]^{\frac{1}{2}}$$

The power coefficient can then be calculated in terms of ζ.

$$P_c = J_1 \cdot \zeta + J_2 \cdot \zeta^2$$

Alternatively if the power is specified the derivatives, J_1' and J_2', are evaluated from $\xi=\xi_0$ to $\xi=1$ and ζ is taken as the positive root of equation 4.15.

$$\zeta = -\frac{J_1}{2 \cdot J_2} + [(\frac{J_1}{2 \cdot J_2})^2 + \frac{P_c}{J_2}]^{1/2}$$

The thrust coefficient can then be calculated in terms of ζ.

$$T_c = I_1 \cdot \zeta - I_2 \cdot \zeta^2$$

4.2 NUMERICAL SOLUTION

As for the analysis routine, the solution to the design equations also entails many computations at each blade element and several deeply nested iterative loops. Therefore to achieve a reasonable accuracy a numerical approach as outlined in steps 1 thru 12 below is necessary.

1) Specify an initial value for the displacement velocity factor, ζ
   Any value will suffice but the more accurate the initial estimate is, the faster the design converges.

2) Calculate ϕ_T, ϕ, F, G

$$\phi_T = \tan^{-1}[(1 + \frac{\zeta}{2}) \cdot \lambda]$$

$$\phi = \tan^{-1}[(1 + \frac{\zeta}{2}) \cdot \frac{\lambda}{\xi}]$$

$$F = \frac{2}{\pi} \cdot [\tan^{-1}(e^{2f} - 1)]^{\frac{1}{2}}$$

$$\textit{where,}\quad f = \frac{B \cdot (1 - r/R)}{2 \cdot \sin(\phi_T)}$$

$$G = F \cdot \frac{\Omega \cdot r}{V} \cdot \cos(\phi) \cdot \sin(\phi)$$

3) Determine angle of attack and lift/drag ratio

$$C_L \rightarrow \alpha \; ; \; \frac{C_D}{C_L}$$

4) Calculate the inflow factors

$$a = (\frac{\zeta}{2}) \cdot \cos^2(\phi) \cdot (1 - \epsilon \cdot \tan(\phi)) \qquad \textit{where,} \quad \zeta = \frac{v'}{V}$$

$$a' = (\frac{\zeta}{2 \cdot X}) \cdot \cos(\phi) \cdot \sin(\phi) \cdot (1 + \frac{\epsilon}{\tan(\phi)}) \qquad \textit{where,} \quad X = \frac{\Omega \cdot r}{V}$$

5) Calculate W, Mach No., Chord, β

$$W = \frac{V \cdot (1 + a)}{\sin(\phi)}$$

$$\textit{Mach No} = \frac{W}{SOS}$$

$$\textit{Chord} = \frac{4 \cdot \pi \cdot V^2 \cdot G \cdot \zeta}{C_L \cdot W \cdot \Omega \cdot B}$$

$$\beta = \alpha + \phi$$

6) Repeat steps 3 through 5 until the Mach number converges (Gauss-Seidel)

7) Calculate the four coefficients

$$I_1' = 4 \cdot \xi \cdot G \cdot (1 - \epsilon \cdot \tan(\phi))$$

$$I_2' = \lambda \cdot (\frac{I_1'}{2 \cdot \xi}) \cdot (1 + \frac{\epsilon}{\tan(\phi)}) \cdot \sin(\phi) \cdot \cos(\phi)$$

$$J_1' = 4 \cdot \xi \cdot G \cdot (1 + \frac{\epsilon}{\tan(\phi)})$$

$$J_2' = \frac{J_1'}{2} \cdot (1 - \epsilon \cdot \tan(\phi)) \cdot \cos^2(\phi)$$

8) Repeat steps 2 through 7 for each blade section

9) Integrate the four coefficients over the entire blade radius

$$I_1 = \int_{\zeta_o}^{1} 4 \cdot \xi \cdot G \cdot (1 - \epsilon \cdot \tan(\phi))$$

$$I_2 = \int_{\zeta_o}^{1} \lambda \cdot (\frac{I_1'}{2 \cdot \xi}) \cdot (1 + \frac{\epsilon}{\tan(\phi)}) \cdot \sin(\phi) \cdot \cos(\phi)$$

$$J_1 = \int_{\zeta_o}^{1} 4 \cdot \xi \cdot G \cdot (1 + \frac{\epsilon}{\tan(\phi)})$$

$$J_2 = \int_{\zeta_o}^{1} \frac{J_1'}{2} \cdot (1 - \epsilon \cdot \tan(\phi)) \cdot \cos^2(\phi)$$

10) Calculate displacement velocity factor, ζ

$$\zeta = \frac{J_1}{2 \cdot J_2} \cdot [(1 + \frac{4 \cdot P_C \cdot J_2}{J_1^2})^{\frac{1}{2}} - 1]$$

11) Repeat steps 2 through 10 until ζ converges (Gauss-Seidel)

12) Calculate Thrust and Efficiency

$$T_C = I_1 \cdot \zeta - I_2 \cdot \zeta^2 \qquad \rightarrow \quad THRUST = T_C \cdot \frac{\rho \cdot V^2 \cdot R^2 \cdot \pi}{2}$$

$$P_C = \frac{2 \cdot POWER}{\pi \cdot \rho \cdot V^3 \cdot R^2} \qquad \rightarrow \quad \eta = \frac{T_C}{P_C}$$

4.2.1 CONVERGENCE CRITERION

Within the design routine an iterative technique has been utilized in two instances. In the first instance the Mach number and its effect on the aerodynamic lift/drag characteristics are assessed and in the second instance the displacement velocity factor, ζ, is required to converge onto a constant value for all blade sections. As these iterative solutions are very stable and converge rapidly a Gauss-Seidel iterative technique with relaxation has been implemented. The Gauss-Seidel technique is straight forward and is very efficient in these instances.

The Mach number defined as the ratio of the relative velocity to the speed of sound, is a measure of compressible flow. As the air flow Mach number over the propeller blade sections increases beyond approximately 0.3, compressibility effects become important, and corrections must be made to the incompressible lift and drag characteristics. A further complication results from the fact that within the design routine it is necessary to manipulate the aerodynamic lift/drag characteristics before the Mach number can be determined. Therefore in a Gauss-Seidel iterative routine the aerodynamic characteristics are assessed and the corresponding Mach numbers are calculated until the Mach numbers converge to within a tolerance of 0.001.

$$\textit{when} \quad |(Mach - Mach_{-1})| > 0.001$$

$$\rightarrow \quad Mach = Mach + W_3 * (Mach_{-1} - Mach)$$

The iterative solution is very stable so a relaxation factor, W_3, of 0.5 is adequate.

The optimum propeller design based upon Betz's helicoidal vortex wake requires that the displacement velocity factor, ζ, is constant along the propeller blades. The governing design equations have thus been developed for a constant displacement velocity and are assessed iteratively. The design routine is initiated with an initial estimate for the displacement factor ζ. The design equations are then assessed and a new ζ value is calculated. If this new ζ value is not within 0.0001 of the initial value, the displacement velocity is modified and the design equations are again assessed.

This process is very stable and is executed very efficiently within a Gauss-Seidel iterative routine.

when $|(\zeta - \zeta_{-1})| > 0.0001$

$$\rightarrow \quad \zeta = \zeta + W_4 * (\zeta_{-1} - \zeta)$$

The technique converges very fast and it has been found that in most circumstances the relaxation factor, W_4, need not be less that one.

4.2.2 BLADE TIP MODIFICATION

According to Prandtl's optimum wake approximation the momentum loss factor, F, is equal to zero at the blade tip. Consequently the blade chord at the tip must also be zero as it is directly proportional to the momentum loss factor.

$$Chord = \frac{4 \cdot \pi \cdot V^2 \cdot G \cdot \zeta}{C_L \cdot W \cdot \Omega \cdot B} \qquad where, \quad G = F \cdot \frac{\Omega \cdot r}{V} \cdot \cos(\phi) \cdot \sin(\phi)$$

$$\rightarrow \quad Chord \propto F$$

Unfortunately a sharp blade tip is often undesirable from a manufacturing and applications standpoint. A propeller with a blunt tip is often required and must therefore be considered in the design. A blunt tip could be accommodated in the design by simply designing the propeller at a slightly larger diameter than required and then manufacturing the blade to the required diameter. In this manner the very thin sections near the propeller tip are eliminated. This approach however is very crude and could be realized much more eloquently by simply modifying the distribution of Prandtl's momentum loss factor, F. As proposed in the analysis section, it is reasonable to assume that the induced velocity in the far wake is in fact finite at the blade tip radius and actually approaches zero at a point just greater than the tip radius. The velocity distribution in the far wake has thus been arbitrarily shifted by 1/100th of the blade diameter and Prandtl's momentum loss factor, F, becomes

$$F = \frac{2}{\pi} \cdot \cos^{-1}(e^{-f})$$

$$f = \frac{B(1 + .005 - r/R)}{2 \cdot \sin(\phi_T)}$$

4.3 VERIFICATION

The design routine was not verified experimentally but instead was verified against the analysis routine. At three different design velocities and design lift coefficients, propellers were designed and then analyzed at the design point. The design parameters were then compared with the parameters determined analytically.

A three bladed, 64 inch diameter propeller with a 14 inch diameter hub, was divided into 12 blade sections. The airfoil sections and corresponding aerodynamic characteristics utilized in this instance, are the same as those determined for the test propeller in Chapter 3. Between blade radii of 7"→12", 12"→20", 20"→26", and 26"→32", the airfoil section characteristics assessed at blade radii of 8", 15", 22", and 30" were utilized respectively. The aerodynamic data was corrected for Mach number effects and assessed at 3000 feet above sea level and 15 degrees celsius. A relaxation factor was not necessary in the design but relaxation factors equal to 0.1, and tolerance levels of 0.1 HP were specified in the analysis.

Shown in Table 6 are the propeller design and analysis parameters corresponding to three different design velocities and lift coefficients. For the propeller designed at 40 knots and a lift coefficient of 0.6, the analysis and design parameters are almost identical. The efficiency of the propeller designed at 40 knots shows the largest discrepancy between the design and analysis, but is relatively insignificant as the analytical efficiency is merely 1.3% less than the design efficiency. The other two propellers designed at 80, and 120 knots and with a lift coefficient of 0.9, show similarly good agreement. It is also interesting to note that even though the design and analysis routines essentially arrive at the same propeller configuration, the analysis routine takes significantly longer to run.

At three different design conditions the design routine has been shown to agree very well with the analysis. Therefore as the analysis routine has been verified experimentally the design routine must also be valid.

Table 6, Design Verfication Against Analytical Parameters

	Des #1	Anal #1	Des #2	Anal #2	Des #3	Anal #3
* Blade RPM	2750	2738.5	2750	2744.5	2750	2745.7
Engine HP	54	54.4	54	54.2	54	54.2
Thrust (lbs)	266.1	264.8	186.5	186.0	134.9	134.6
Effic (%)	60.5	59.7	84.8	84.3	92.1	91.5
C_L Range	.6 → .6	.6 → .61	.9 → .9	.9 → .91	.9 → .9	.9 → .91
Process Time (s)	7.8	18.9	5.0	18.8	3.9	21.4

Des #1 : Design Velocity = 40 knots

Des #2 : Design Velocity = 80 knots

Des #3 : Design Velocity = 120 knots

* Reduction Gear = 2.58 (ie. Engine RPM = 2.58 * Blade RPM)

4.4 OPTIMIZATION

The design methodology developed herein can be utilized to design a propeller to operate with optimal efficiency at one operating point. Most often however, the propeller must operate efficiently over a wide range of forward velocities. To accommodate this requirement in the design process an iterative routine based on both the design and analysis routines has been implemented. A propeller is designed at a particular operating point and then analyzed over the entire operating range. If the overall performance characteristics are not sufficient then the propeller is redesigned at a more appropriate operating point and again analyzed over the full operating range. This iterative process will eventually produce an adequate propeller design but it could require several iterations. A structured approach has therefore been introduced such that the most appropriate design can be obtained with a minimal number of iterations.

In the first instance the design forward velocity corresponding to the best overall performance is required and is most readily determined by means of a graphical trial and error process. Propellers are designed at several forward velocities, analyzed over the full operating range, and then the overall performance characteristics are compared. The design velocity corresponding to the best performance curve is then noted and if necessary used as a pivot for a further refinement. That is, propellers are again designed and analyzed but this time at velocities in the near vicinity of the design velocity just determined. The number of iterations required will depend on the grid sizes and the required accuracy but generally no more than two or three iterations should be necessary. Furthermore as the optimum design velocity is generally found to be approximately ten to twenty percent lower than the maximum velocity, a significant reduction in computational time is realized if the pivot velocity in the first iteration is taken as approximately eighty five percent of the maximum forward velocity. Additionally, in order that the graphical comparisons are solely representative of design forward velocity, all the design parameters with the exception of the design forward velocity and lift coefficient, must be constant throughout the iterative process. Only the lift coefficient is considered an independent variable such that the blade chords can be limited to practical lengths. The design engine rotational velocity should correspond with the

maximum engine power, as ideally the engine should operate near this optimum over most of the aircraft's operating range

As off-design performance is not considered within the classical design routine it is safe to assume that the propeller will perform most efficiently at conditions near the design point. If the best performance is required at lower velocities then the propeller should be designed at a relatively low forward velocity. Likewise if the best performance is required at higher velocities the propeller should also be designed at a relatively high forward velocity. Alternatively if the propeller is required to perform well at both high and low forward velocities, the design forward velocity should be somewhere between the two extremities. Unfortunately the blade twist corresponding to such a design is likely to promote blade stall and therefore performance degradation at both the low and high velocities. The best approach to optimization in this instance is then to design the propeller at the lowest possible forward velocity which just meets the upper performance requirement, or alternatively design the propeller at the maximum possible velocity which just meets the lower performance requirement.

A further refinement to the optimization process is realized through consideration of the propeller rotational velocity and the coefficient of lift. As poor performance at relatively low velocities is due mainly to blade stall, the performance could be improved by decreasing the aerodynamic angle of attack. Therefore as the angle of attack is inversely proportional to the blade rotational velocity and directly proportional to the coefficient of lift, the blade rotational velocity should be maximized and the coefficient of lift minimized. The maximum tip Mach number and blade chords must therefore be carefully assessed as they limit the rotational velocity and coefficient of lift.

Propellers are often installed just upstream of engine nacelles so to truly design an optimum propeller the flow field as modified by the nacelle must be considered. Unfortunately the classical design routine is based upon a helicoidal trailing vortex wake of constant displacement velocity and therefore cannot accommodate the modified flow field. That is the radially variable axial free-stream velocity introduced by the nacelle is inconsistent with a constant displacement velocity. Lacking a more elaborate vortex wake model, the nacelle effects can then only be assessed by means of analysis.

Chapter 5

Light Aircraft Application

5.0 LIGHT AIRCRAFT APPLICATION

The design and analysis routines that have been developed in Chapters three and four respectively, are based on several light loading approximations. For instance Prandtl's momentum loss approximation has been utilized but it only approximates Goldstein's exact solution when the trailing vortex sheets are spaced relatively close to one another. As the vortex sheet spacing is proportional to the propeller loading the propeller must therefore be lightly loaded. The light loading requirement can be accommodated by using a large number of blades but for the most part only two or three blades are necessary in most light aircraft applications. Based upon a light loading and taking into account all the design constraints and requirements, an optimum propeller suitable for a light aircraft has been designed and analyzed.

5.1 DESIGN REQUIREMENTS

The aircraft for which the propeller is to be designed has a very wide operating range of thirty nine to one hundred and seventy five knots. A variable pitch propeller would most likely give the best overall performance but for sake of simplicity and cost, a two bladed fixed pitch propeller was preferable. The maximum propeller diameter as determined by the aircraft geometry is five feet and the hub diameter is specified as fourteen inches.

The engine utilized in this instance is a Subaru and its performance characteristics are approximated in Figure 34. As this performance data supplied by the engine manufacturer was determined at sea level atmospheric conditions, standard corrections for altitude and temperature are incorporated into the design and analysis routines. Also from Figure 34 it is seen that the engine does not operate efficiently at rotational velocities less that 3500 RPM. Furthermore to sustain a high engine reliability with minimal maintenance the engine rotational velocity has been limited to a maximum of 5500 RPM. The engine is therefore confined to a rotational velocity range of 3500 to 5500 RPM and the propeller must be designed accordingly.

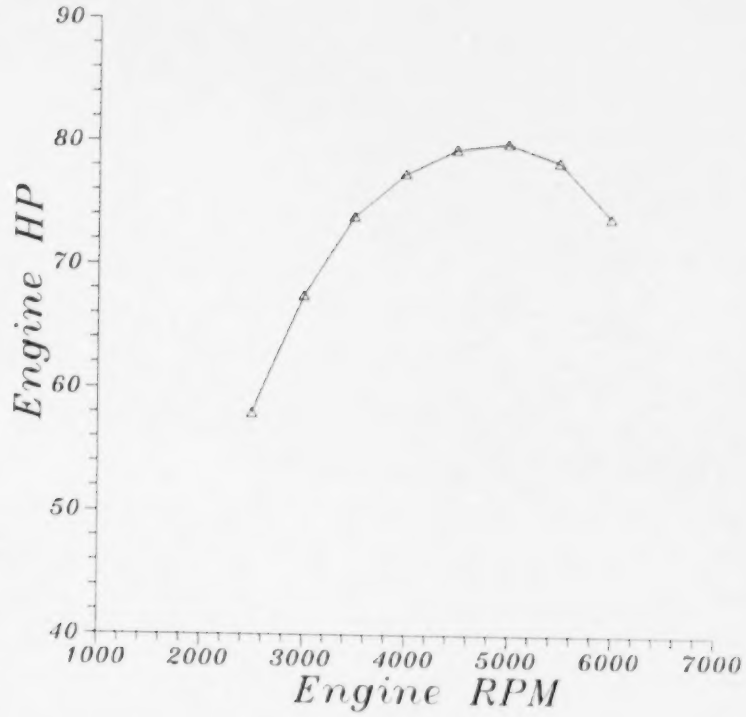

Figure 34, Subaru Engine Performance Curve

The design and analysis routines are based extensively upon the aerodynamic characteristics at each blade element. Therefore the accuracy of the routines depends primarily upon the accuracy of the aerodynamic data. Unfortunately, accurate airfoil characteristics pertaining to the flow around rotating propeller blades are very difficult to obtain. In fact, full scale wind tunnel tests are often the only means of obtaining representative data, particularly at stalled conditions. The scope of this research did not entail intensive wind tunnel testing so it was necessary to rely on published airfoil data.

Several airfoil families such as the NACA-16, ARA-D, and EPP-850 have been developed for propellers and are discussed in references [29,30,31]. The NACA-16 is a very popular series but it was felt that a more modern series such as the ARA-D

was more efficient and would therefore result in better propeller performance. Unfortunately only a few aerodynamic characteristics of the ARA-D series have been published and therefore the full series could not be utilized. Published aerodynamic data was available for the Eppler 850 series shown in Figure 35 and was therefore utilized in this propeller design. Between blade radii of 7"→10", 10"→14.5", 14.5"→19", 19"→23.5", 23.5"→28", and 28"→30" Eppler's 850, 851, 853, 855, 856, and 857 sections have been utilized respectively. The lift and drag characteristics are shown in Figure 36 and as the airfoil stall characteristics have not been determined they are approximated with sine and cosine functions.

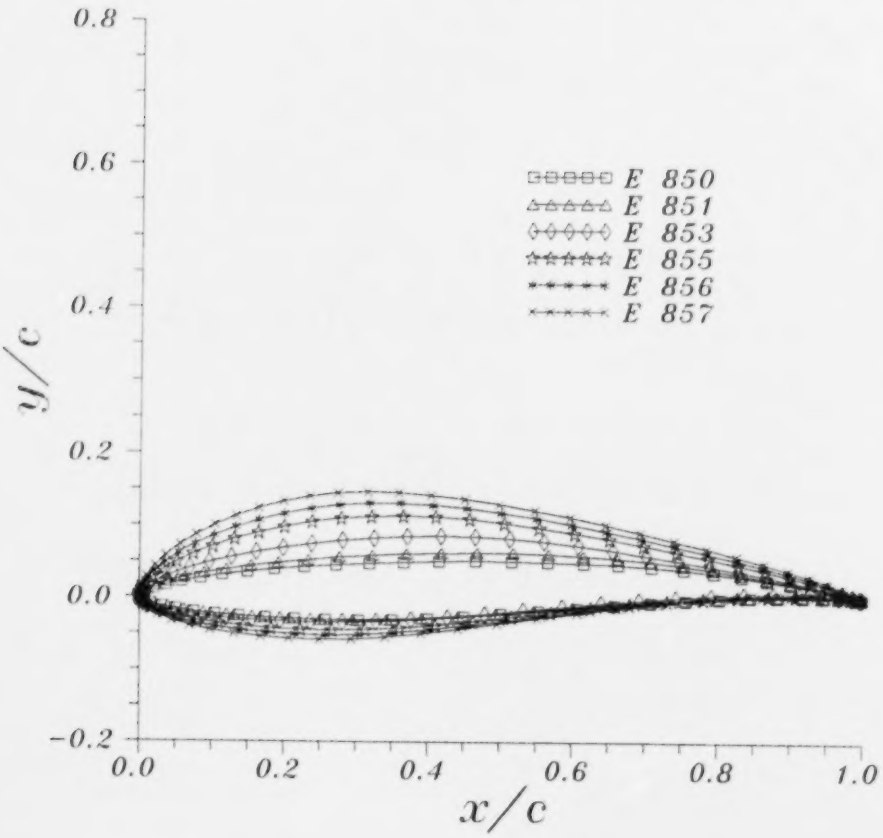

Figure 35, Blade Airfoil Coordinates (Eppler 850 Series)

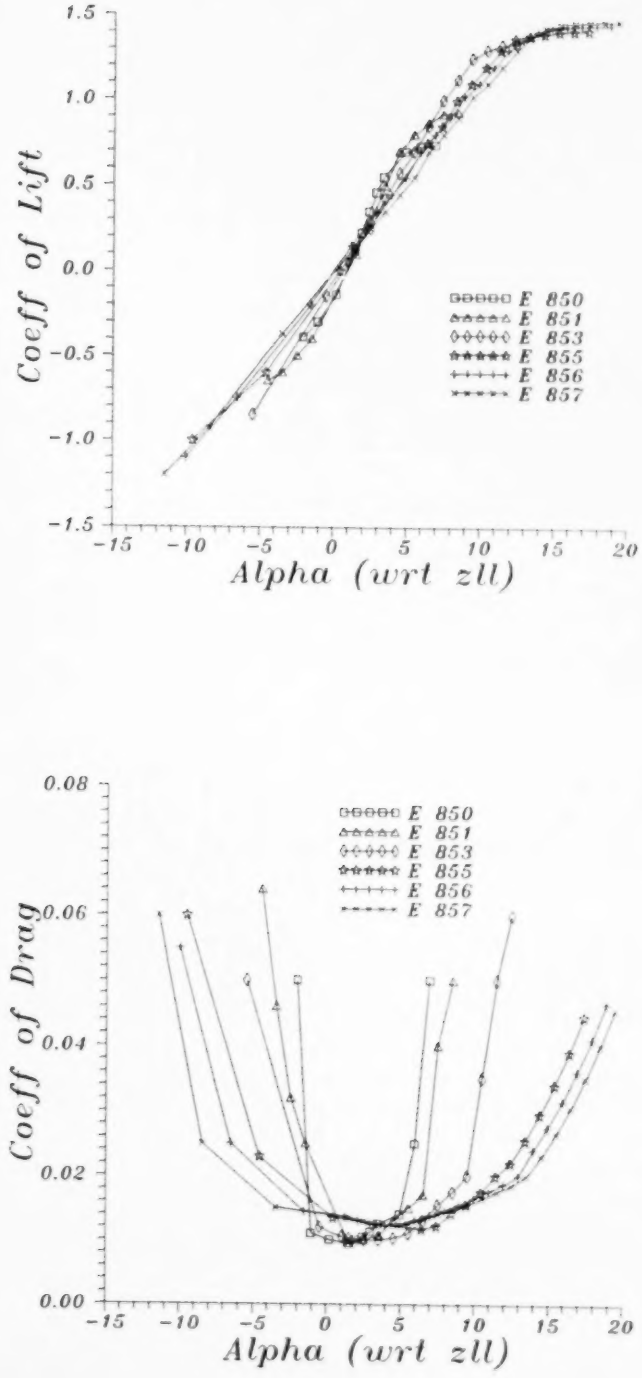

Figure 36, Lift and Drag Characteristics (Eppler 850 Series)

5.2 OPTIMUM DESIGN

Both the design and analysis routines have been utilized in the optimization process. Propellers are designed at a variety of operating conditions and by means of the analysis, the corresponding performance characteristics are assessed over the full operating range of the aircraft.

An engine reduction gear ratio of 1:64 was specified and the design engine rotational velocity of 4500 RPM was specified to correspond with the maximum engine power. Also as the aircraft was to operate at a maximum forward velocity of 175 knots the initial pivot velocity (design) was taken at approximately eighty five percent of this value, 140 knots. About this pivot velocity at increments of ten knots, propeller blade geometries corresponding to optimum efficiency were designed. Based upon a maximum chord of 5.7 inches design lift coefficients of .65, .55, .47, .4, and .35 were required at design forward velocities of 110, 125, 140, 155, and 170 knots respectively. The propellers were then analyzed over the full operating range of the aircraft and the performance curves for each propeller design are shown in Figure 37.

The poor performance characteristics at forward velocities less than 75 knots are caused by aerodynamic stall occurring over a significant portion of the propeller blades. Blade stall introduces a large drag component which significantly degrades the propeller performance and also introduces uncertainties into the calculated performance values. At velocities less than approximately 25 knots, high performance is not essential as the aircraft is merely in a taxiing mode and therefore a fully stalled blade is permissable. However between 25 and 75 knots the aircraft is in take off and climb mode which requires the best possible propeller performance and therefore a fully stalled blade is unacceptable. To minimize the blade stall at these low forward velocities the propeller must be designed at the lowest possible velocity and lift coefficient, while at the same time ensuring that the upper performance requirement is satisfied.

In this instance the upper performance requirement was dictated by the maximum engine rotational velocity of 5500 RPM and the maximum forward velocity of 175 knots. Again considering the performance curves in Figure 37 it was seen that the propeller designed at 125 knots just meets the design requirement. That is at a forward velocity

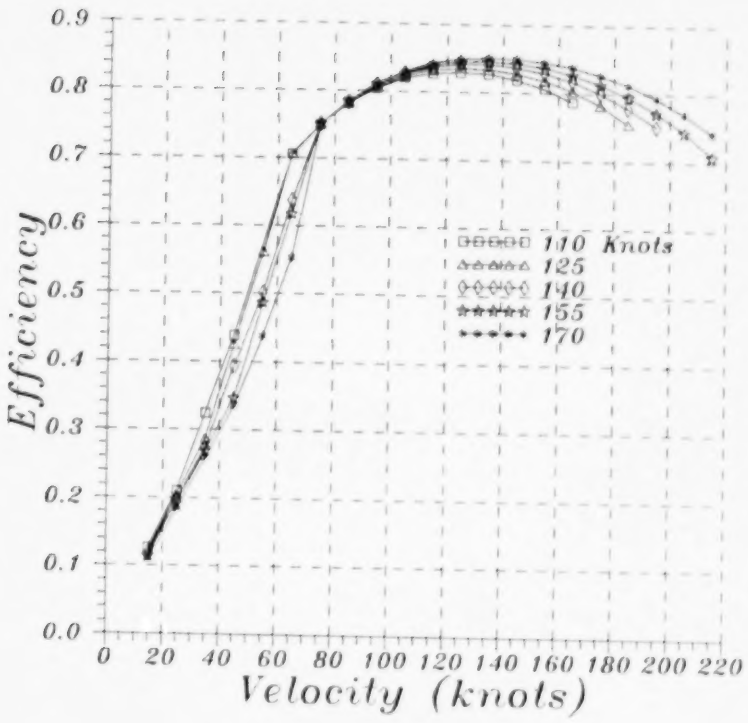

Figure 37, Performance Curves for Design Iteration #1

of 175 knots the propeller designed at 110 knots exceeds the maximum engine rotational velocity and the propeller designed at 140 knots falls short of the maximum engine rotational velocity.

Having determined that a design velocity of 125 knots produces the best overall performance, the optimization process was further refined by selecting the pivot velocity as 125 knots in a second iteration. About this pivot velocity at increments of 5 knots, propellers were then designed and analyzed over the full operating range of the aircraft. Again maintaining a maximum chord of approximately 5.7 inches, radially constant lift coefficients of .63, .59, .55, .52, and .49 were required at the design velocities of 115, 120, 125, 130, and 135 knots respectively. Neither of these propeller designs exceeded

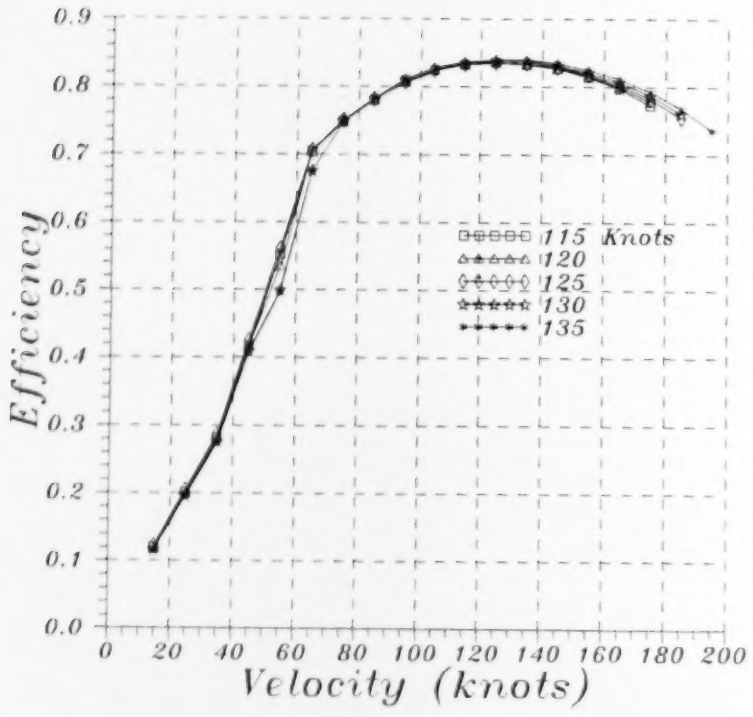

Figure 38, Performance Curves for Design Iteration #2

the maximum engine rotational velocity and as shown in Figure 38 the performance curves are very similar. If this was the last step in the optimization process the design velocity of 115 knots would be considered optimum as the corresponding engine rotational velocity is just 0.3% less than the maximum. That is the velocity could not be reduced any further as the engine rotational velocity would then be too large at a forward velocity of 175 knots. However in this instance one further iteration has been undertaken and therefore the design velocity of 125 knots was chosen such that the blade rotational velocity could be allowed to increases slightly, if necessary.

By designing the propeller at the lowest possible forward velocity some high end performance was inevitably compromised for significant gains in low end performance. The lower design velocity translates to smaller blade angles and therefore less severe stall

at low forward velocities. However, the propeller designed at the relatively low velocity of 125 knots is still partially stalled at forward velocities less than 65 knots. The stall is particularly severe near the blade tips but could possibly be minimized by reconsidering the distribution of the design lift coefficients. If the design lift coefficient is decreased slightly near the tip, the corresponding design angle of attack also decreases thereby minimizing the severity of tip stall at the slower velocities. At a design velocity of 125 knots the design lift coefficient distribution has thus been reduced near the blade tip. The lift coefficients vary linearly between the values specified at the blade root and blade tip and therefore to maintain the maximum chord of 5.7 inches the lift coefficient at the blade root was necessarily increased. The performance curves for the four coefficient of lift ranges considered; 0.55→0.55, 0.58→0.45, 0.61→0.35, and 0.65→0.25; are shown in Figure 39.

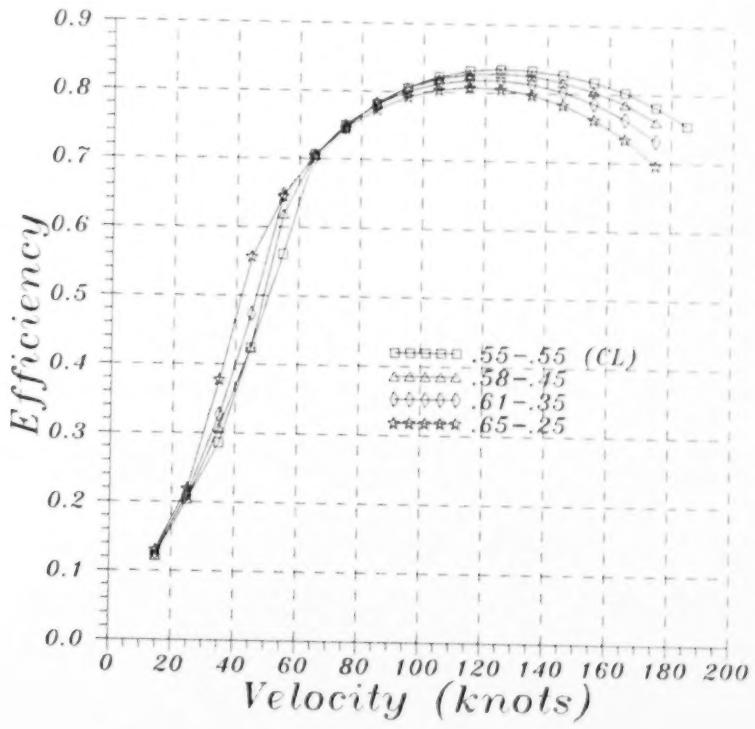

Figure 39, Performance Curves for Design Iteration #3

Neither of these propeller designs exceeded the maximum engine rotational velocity but the performance curves are significantly different. The propeller designed with a radially constant lift coefficient has the best performance at a forward velocity of 175 knots. On the other hand the propeller designed with a lift coefficient ranging from 0.65 at the blade root to 0.25 and the blade tip, has the best performance at forward velocities less than 65 knots. In this instance the latter propeller design is preferable as even though the efficiency at 175 knots is only approximately 70%, the performance at velocities less than 65 knots is acceptable.

Lastly it is necessary to consider the choice of engine reduction gear. If the reduction gear ratio of 1:1.64 were reduced the propeller would rotate faster and the blade angles would decrease thereby increasing the low end performance. Unfortunately as the engine rotational velocity is already at a maximum for a ratio of 1:1.64, the engine rotational velocity and tip Mach number would likely exceed the maximum allowable at a smaller ratio. Therefore the ratio of 1:1.64 is sufficient.

5.2.1 BLADE GEOMETRY

Based on the optimum design parameters determined above, the appropriate propeller geometry has been calculated. The propeller geometry is sufficiently represented by the blade angle, β, and the blade chord.

The blade angle, β, is calculated with respect to the zero lift of the element airfoil sections and is shown as a function of blade radius in Figure 40. The blade angle of 60.5 degrees at the blade root is quite large in comparison to the 20 degree angle at the blade tip. The unusually large twist would be reduced if nacelle interference was taken into account for this particular propeller design. The classical design methodology does not allow for nacelle interference, but if it did the twist as designed would be significantly less.

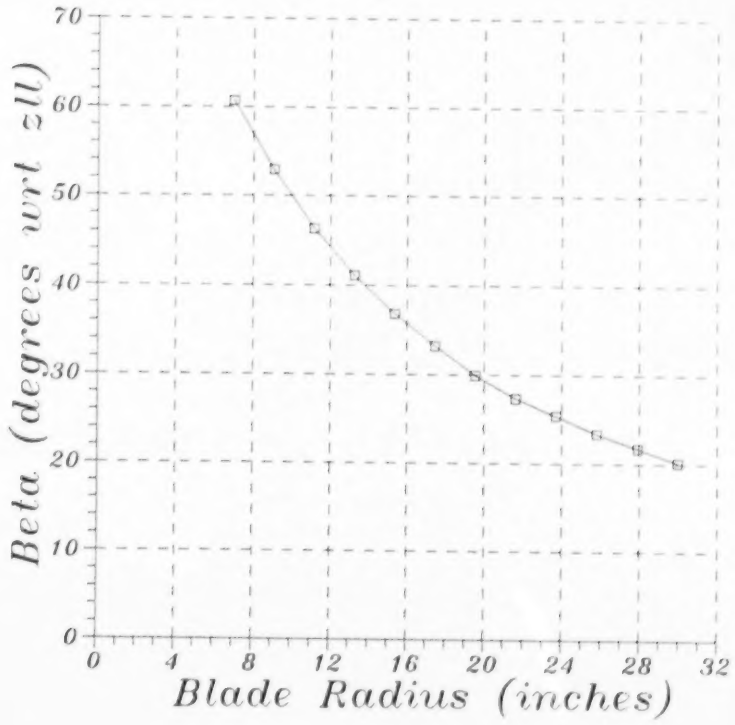

Figure 40, Blade Angle as Designed

The blade chords are designed such that with the specified lift coefficients and corresponding blade angles, the trailing vortex wake moves rearwards with a constant displacement velocity. The blade chords have been determined as a function of blade radius as shown in Figure 41, and the distribution is typical of optimally designed propellers.

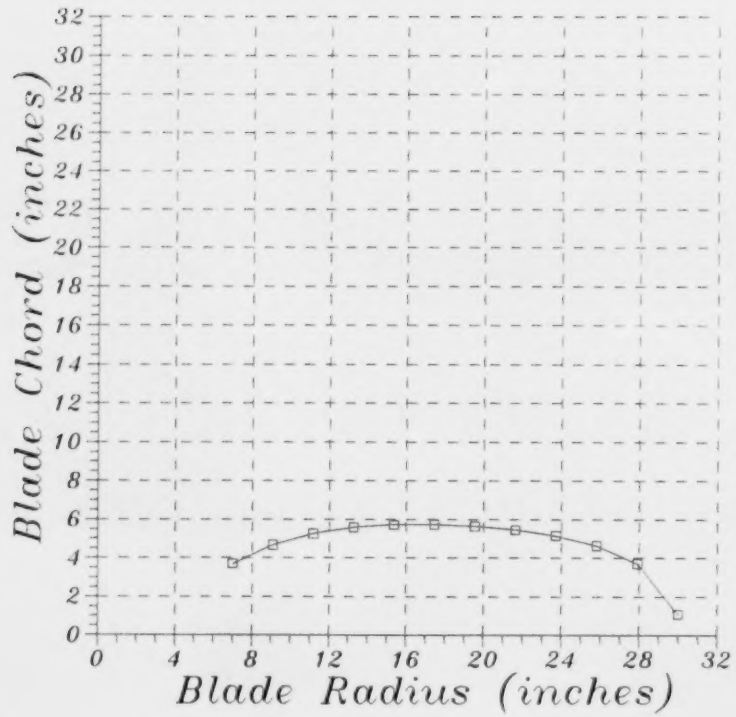

Figure 41, Blade Chord as Designed

5.2.2 PERFORMANCE CHARACTERISTICS

The propeller as designed has been analyzed over the full operating range of the aircraft. As shown in Table 7 the vortex sheet spacing is less than or equal to the blade tip radius for all the forward velocities considered. The light loading assumptions are therefore valid as well as all the propeller performance characteristics shown in figures 42 thru 49. The maximum propeller efficiency of 81% is obtained at 115 knots, but the predominant benefit of this design is that over most of the operating range, 60 to 175 knots, the efficiency is greater than 70%. The engine RPM does not exceed 5500 RPM, the maximum tip Mach number of 0.83 is acceptable, and the thrust and torque curves are reasonable.

The performance characteristics at velocities greater than 60 knots are quite typical of optimum propellers, but at velocities less than 60 knots the propeller blades begin to stall and a significant variance from the general trend occurs. Some of the variance can be attributed to inaccurate aerodynamic stall data but for the most part it is simply due to the stall characteristics. Consider for example the blade RPM as a function of forward velocity shown in figure 44. As the velocity decreases from 175 knots to 75 knots the angle of attack and the corresponding lift coefficients increase respectively. As a result the torque component of the lift is also increased and therefore the engine rotational velocity must decrease until the power required by the propeller matches that supplied by the engine. However, as the forward velocity is further decreased from 75 knots to 65 knots the engine rotational velocity is seen to increase. This local trend reversal is due to the fact that the lift coefficients and the corresponding torque components are somewhat reduced by partial blade stall. Therefore the engine rotational velocity must increase until the power required by the propeller matches that supplied by the engine. As the forward velocity is further decreased from 45 knots down to 15 knots the local engine rotational velocity again decreases, but in this instance is attributable to relatively large drag coefficients.

The performance characteristics at velocities less than 75 knots can be rationalized but the fact remains that they are based upon approximate aerodynamic stall data. These performance characteristics must then be looked upon with some discretion.

Table 7, Advance Ratio and Vortex Sheet Spacing

Forward Velocity (knots)	Advance Ratio (J=V/nD)	Vortex Sheet Spacing * (b/r)
15	0.138	0.138
25	0.232	0.231
35	0.306	0.305
45	0.380	0.377
55	0.470	0.465
65	0.564	0.555
75	0.645	0.632
85	0.714	0.696
95	0.777	0.754
105	0.832	0.804
115	0.881	0.848
125	0.924	0.886
135	0.961	0.919
145	0.994	0.948
155	1.022	0.972
165	1.047	0.993
175	1.069	1.012

* $\frac{b}{R} = \frac{2\pi}{B}\frac{\lambda}{\sqrt{\lambda^2+1}}$ *where,* $\lambda = \frac{V}{\Omega \cdot R} = \frac{J}{\pi}$

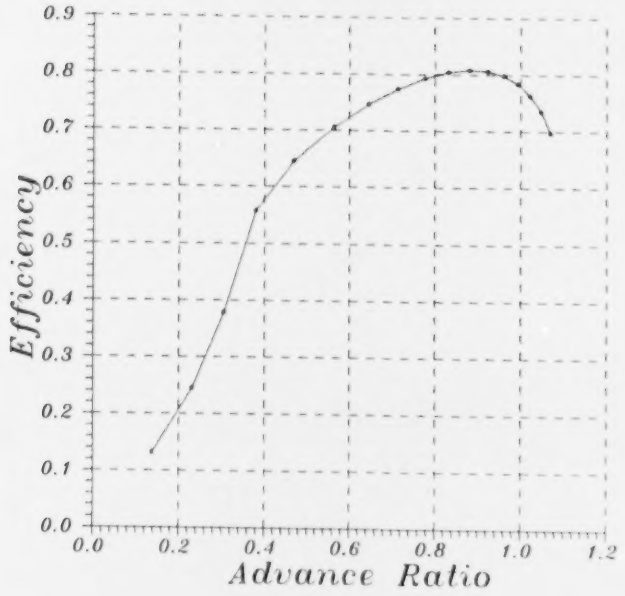

Figure 42, Propeller Efficiency vs. Advance Ratio

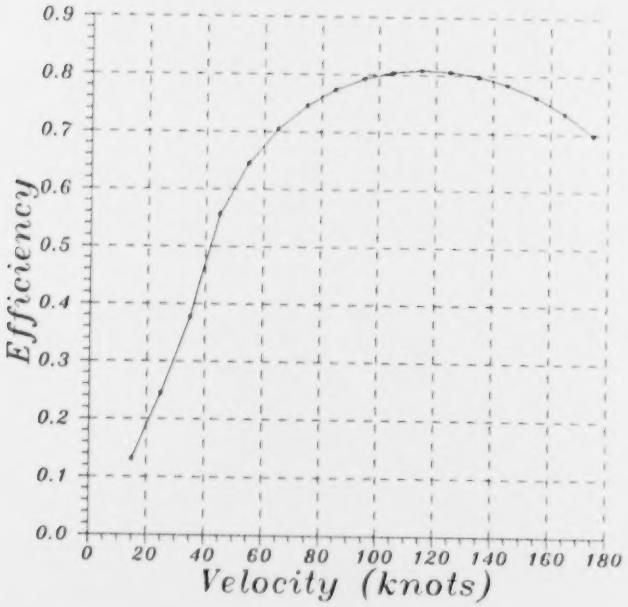

Figure 43, Propeller Efficiency vs. Forward Velocity

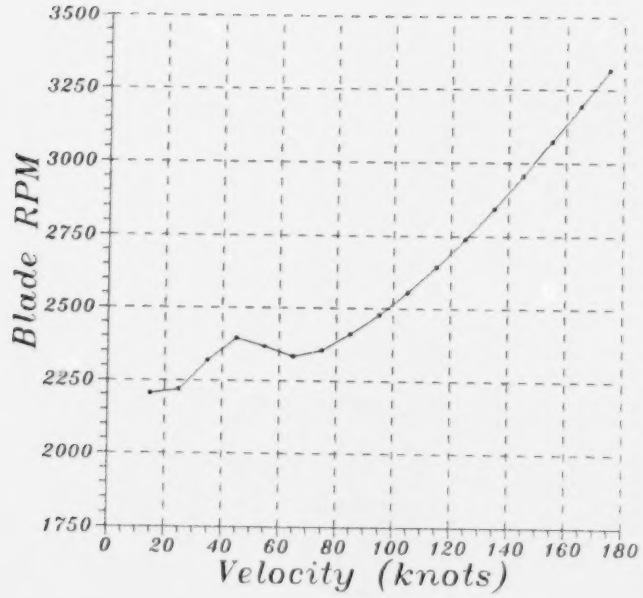

Figure 44, Blade RPM vs. Forward Velocity

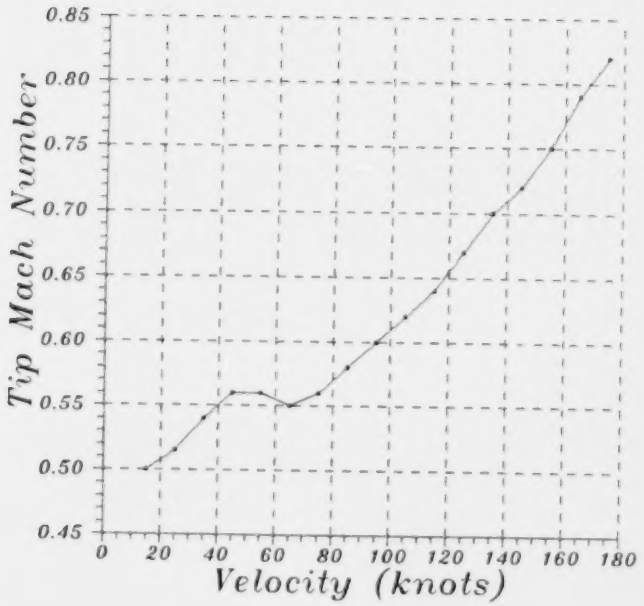

Figure 45, Blade Tip Mach Number vs. Forward Velocity

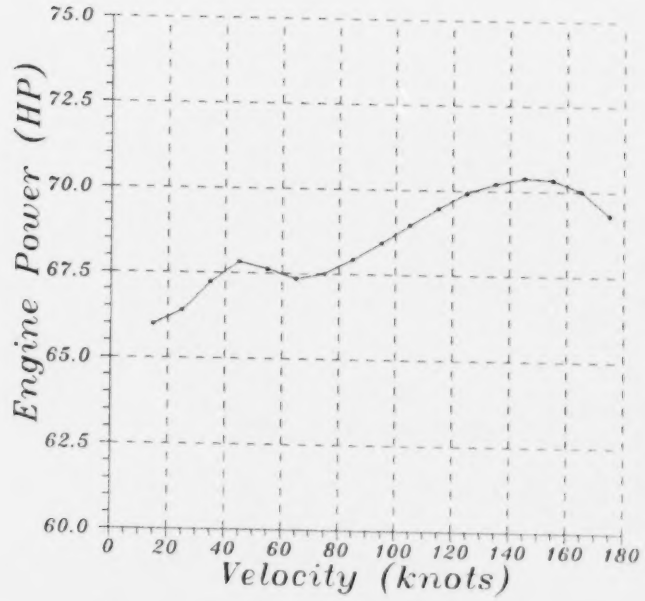

Figure 46, Engine Power vs. Forward Velocity

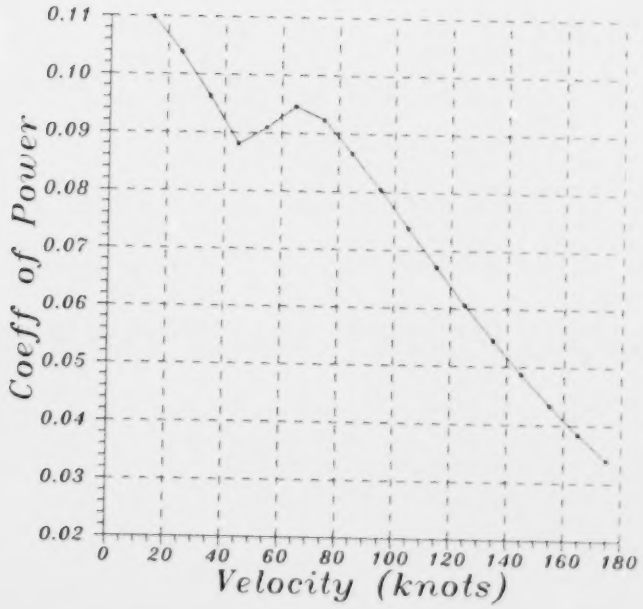

Figure 47, Coefficient of Power vs. Forward Velocity

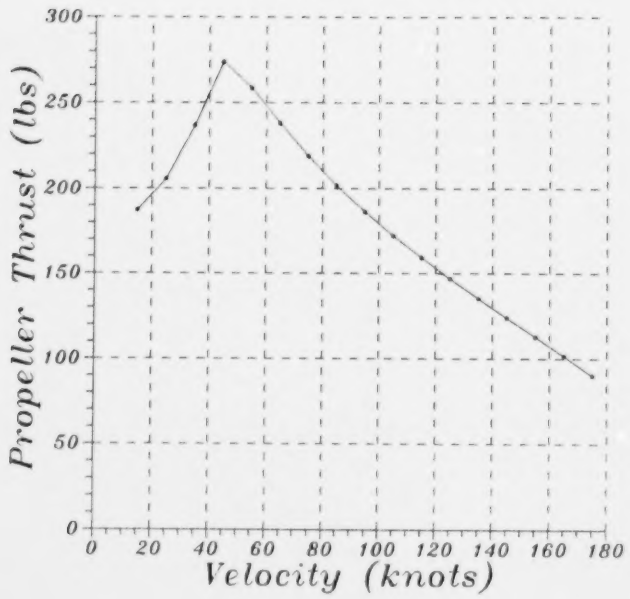

Figure 48, Propeller Thrust vs. Forward Velocity

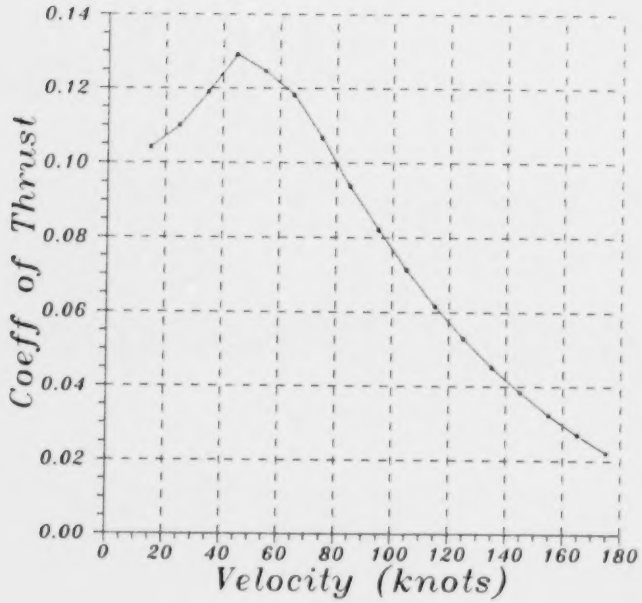

Figure 49, Coefficient of Thrust vs. Forward Velocity

Chapter 6

Conclusions

6.0 CONCLUSIONS

Analysis and design methodologies based upon classical propeller theory have been developed. Momentum and blade element theory have been integrated into both an iterative numerical analysis routine based upon the velocity inflow factors and an iterative numerical design routine based upon a constant displacement velocity. The design routine converges very quickly and a relaxation factor is not required. The analysis routine on the other hand requires a relatively small relaxation factor to eliminate instabilities and therefore it converges more slowly than the design.

The routines have been developed for lightly loaded propellers and Prandtl's approximate induced velocity distribution has been utilized. To improve convergence of the analysis routine near the blade tips, Prandtl's momentum loss distribution was shifted radially thereby implying a non-zero momentum loss factor at the tip. Prandtl's momentum loss distribution was also shifted radially in the design routine so as to ensure a finite chord at the blade tip.

The two dimensional airfoil data was corrected for compressibility effects and the aerodynamic stall characteristics were approximated with sine and cosine functions. Also the engine nacelle was modelled in the analysis routine as an axi-symmetric body.

6.1 VALIDATION OF THE ANALYSIS AND DESIGN ROUTINES

A three bladed fixed pitch propeller was analyzed and tested over the operating range of a light aircraft. The propeller RPM were used as a basis for comparison and it was found that the measured RPM was at most 6.3% greater than the analytical RPM. A 6.3% error is acceptable upon considering that Prandtl's light loading approximation is only within 18% of the exact solution. The trailing vortex sheet spacing was significantly less than the propeller radius so the error in the light loading approximation was actually less than 18% but likely greater than 6.3%. Error can also be attributed to engine nacelle interference corrections and inaccurate aerodynamic stall data.

The design routine was not verified experimentally but instead was verified against the analysis routine. The design was found to be in exact agreement with the analysis at the design point and as the analysis was experimentally verified, the design must also be valid.

6.2 DESIGN AND ANALYSIS OF A LIGHT AIRCRAFT PROPELLER

Integrating both the design and analysis routines into an optimization process, an optimum propeller suitable for a light aircraft was designed. Three optimization iterations were required before the propeller best suited for the light aircraft could be determined. After the first iteration it was apparent that the performance at the lower forward velocities was severely inhibited by blade stall. The propeller twist as designed was thus minimized by designing the propeller at the lowest possible forward velocity. It was found that the minimum velocity the propeller could be designed for without exceeding the light loading limitation ($b/R \leq 1$), the maximum tip Mach number, and the maximum engine rotational velocity was 125 knots. Furthermore the blade tip stall was minimal for a design lift coefficient ranging from 0.65 at the blade root to 0.25 at the blade tip.

As the propeller was required to operate efficiently over the full operating range of 39 to 175 knots, the efficiency was not maximized at a particular operating point but rather was levelled off over most of the operating range. A maximum efficiency of only 80.5% was obtained at 115 knots but from 65 knots to 175 knots the efficiency was greater than 70%. At forward velocities less than 45 knots the efficiency drops off significantly but as accurate aerodynamic stall data was not available the calculated performance characteristics in this velocity range must be considered with some discretion.

6.3 FURTHER RESEARCH

The calculated performance characteristics are typical of lightly loaded and optimally designed propellers. It is conceivable however that the accuracy could be improved for both the analysis and design routines by accurately determining the propeller aerodynamic characteristics and in particular the stall characteristics.

Airfoil analysis methods are generally invalid at stall conditions so wind tunnel tests of all the blade sections are necessary to accurately determine the stall characteristics of the propeller blades. The Reynold's number and Mach number should be modelled accurately and the blade airfoil sections should be tested at large angles of attack.

It should be noted however that two dimensional airfoil data obtained in standard wind tunnel tests does approximate the flow around a propeller blade, but does not account for radial flow along the propeller blades. The effect that this radial flow has on the blade aerodynamics is uncertain and is therefore best determined experimentally.

BIBLIOGRAPHY

[1] Foley, William M., "From DaVinci to the Present - A Review of Airscrew Theory for Helicopters, Propellers, Windmills and Engines", AIAA Paper No. 76-367

[2] Hassell, Patrick, "Propeller Aerodynamics - A U.K. Perspective - The First Hundred Years", Dowty Aerospace Ltd.

[3] Bass, R.M., "Historical Review of Propeller Developments", Lecture Series 1982-08, Von Karman Institute for Fluid Dynamics

[4] Drzewiecki, S., "Des Helices Ariennes", Paris, 1909

[5] Rankine, W.J.M., "On the Mechanical Principles of the Screw Propeller", Reprinted as ARC R&M 64, 1911

[6] Froude, R.E., "On the Part Played in Propulsion by Differences of Fluid Pressure", Trans. Inst. of Naval Architects, Vol 30, 1889

[7] Glauert, H., "Airplane Propellers", Aerodynamic Theory, Vol.4, Editor-in-Chief W. F. Durand, 1976, p.261

[8] Betz, A., "Screw Propellers with Minimum Loss of Energy", Göttinger Nachr, 1919, p.193

[9] Betz, A., Handbuch der Physik, Vol.7, 1927, p.256

[10] Appendix to Betz's paper, Göttinger Nachr, 1919, p.193

[11] Lock, C. N. H., "The Application of Goldstein's Theory to the Practical Design of Airscrews", Reports and Memoranda No. 1377, Nov 1930

[12] Goldstein, S., "On the Vortex Theory of Screw Propellers", Roy. Soc. Proc. (A), 123,440, 1929

[13] Theodorsen, T., "Theory of Propellers", McGraw Hill Book Co., New York, 1948

[14] Theodorsen, T., "Theory of Static Propellers and Helicopter Rotors", 25th Annual National Forum Paper No. 326, American Helicopter Society, May 1969

[15] Theodorsen, T., "Theory of Propellers", Parts I & II, NACA Technical Reports No. 776 & 777

[16] Munk, "Isoperimetrische Aufgaben aus der Theorie des Fluges", Göttingen, Dissertation, 1919

[17] Stepniewski and Keys, "Rotary Wing Aerodynamics", Dover 1984

[18] Larabee, E. E., "Practical Design of Minimum Induced Loss Propellers", SAE Paper 790585

[19] Breeze-Stringfellow, A., "Computation of Propeller Nacelle Interference Flows Using Streamtube Coordinates", Applied Mechanics, Bioengineering, and Fluids Engineering Conference, Houston Texas, June 1983

[20] Karamcheti, Krishnamurty, "Principles of Ideal-Fluid Aerodynamics", John Wiley & Sons, 1966

[21] Landgrebe, A.J. and Cheney, M.C., "Rotor Wakes - Key to Performance Prediction", AGARD Fluid Dynamics Panel Conference Proceedings, No. 111, Feb 1973

[22] Adkins, C.N., "Design of Optimum Propellers", AIAA Paper 83-0190

[23] Willson, R. and Lissmann, P., "Applied Aerodynamics of Wind Power Machines", Oregon State University, NSF/RA/N-74-113, PB-239595/3, July 1974

[24] Viterna, A. and Janetzke, D., "Theoretical and Experimental Power from Large Horizontal-Axis Wind Turbines", Proceedings from the Large Horizontal-Axis Wind Turbine Conference, DOE/NASA-LeRC, July 1981

[25] Larabee, E.E., "A Pictorial Acccount of the Fundamentals of Propeller Theory and its Applicatoin to the Design of a Pedal Driven Airplane Propeller, Massachusetts Inst. of Techn., January 1980

[26] Houghton, E.L. and Carruthers, N.B., "Aerodynamics for Engineering Students", 3rd Edition, Edward Arnold Pty Ltd., ISBN 0-7131-3433-X, 1982

[27] Kennedy, J.L. and Marsden, D.J., "Potential Flow Velocity Distribution on Multi-Component Sections", Canadian Aeronautics and Space Journal, Vol. 22, No. 5, 1976, pp. 243-256

[28] Kennedy, J.L., "The Design and Analysis of Airfoil Sections", Ph.D. Thesis, University of Alberta, 1977

[29] Lindsey, W.F., Stevenson, D.B., and Daley, B.N., "Aerodynamic Characteristics of 24 NACA 16-Series Airfoils at Mach Numbers Between 0.3 and 0.8", NACA Technical Note, No. 1548, September 1948

[30] Bocci, A.J., "A New Series of Aerofoil Sections Suitable for Aircraft Propellers", The Aeronautical Quarterly, Vol. 27, pp. 55, February 1977

[31] Eppler, "Airfoil Design and Data", Springer-Verlag, 1990, ISBN 0-387-52505-X

APPENDIX

A.1 OPTIMUM CIRCULATION DISTRIBUTIONS

Table A1, Optimum Circulation Functions (2 Blades)

($\mu_0 = 2 \Rightarrow \lambda = .5 \Rightarrow J = 1.57$)

	Goldstein		Prandtl		
r/R	μ_o	G	f	F	G
0	0	0	2.24	.932	0
.1	.2	.092	2.01	.915	.035
.2	.4	.175	1.79	.893	.123
.3	.6	.243	1.57	.866	.229
.4	.8	.295	1.34	.832	.325
.5	1.0	.329	1.12	.788	.394
.6	1.2	.341	0.89	.732	.432
.7	1.4	.331	0.67	.658	.436
.8	1.6	.295	0.45	.558	.402
.9	1.8	.220	0.22	.410	.313
1	2.0	0	0	0	0

$$\lambda = \frac{V}{\Omega \cdot R} = \frac{1}{\mu_0} \qquad J = \lambda \cdot \pi \qquad r/R = \lambda \cdot \mu_0$$

$$f = \frac{B}{2} \frac{\sqrt{\lambda^2 + 1}}{\lambda} \left(1 - \frac{r}{R}\right)$$

$$F = \frac{2}{\pi} \cos^{-1}(e^{-f}) = \frac{2}{\pi} \tan^{-1}\left(\sqrt{e^{2f} - 1}\right)$$

$$G_{Prandtl} = \frac{B \cdot \Omega \cdot \Gamma}{2\pi \cdot V \cdot v'} = F \frac{\chi}{\chi^2 + 1} \qquad , \text{ where } \chi = \frac{\Omega r}{V}$$

$$G_{Goldstein} = \frac{B \cdot \Omega \cdot \Gamma}{2\pi \cdot V \cdot v'} \qquad [Ref\ Goldstein,\ 10]$$

Table A2, Optimum Circulation Functions (2 Blades)

($\mu_0 = 3 \Rightarrow \lambda = .333 \Rightarrow J = 1.05$)

	Goldstein		Prandtl		
r/R	μ_o	G	f	F	G
0	0	0	3.162	.973	0
.0667	.2	.111	2.951	.967	.037
.1333	.4	.213	2.741	.959	.132
.2	.6	.303	2.530	.949	.251
.2667	.8	.379	2.319	.937	.366
.3333	1.0	.440	2.108	.922	.461
.4	1.2	.485	1.897	.904	.534
.4667	1.4	.514	1.686	.881	.584
.5333	1.6	.533	1.476	.853	.614
.6	1.8	.537	1.265	.818	.625
.6667	2.0	.525	1.054	.773	.619
.8333	2.5	.427	0.527	.598	.516
.9333	2.8	.303	0.211	.399	.354
1.0	3.0	0	0	0	0

Table A3, Optimum Circulation Functions (2 Blades)

($\mu_0 = 4 \Rightarrow \lambda = .25 \Rightarrow J = .785$)

	Goldstein		Prandtl		
r/R	μ_o	G	f	F	G
0	0	0	4.123	.990	0
.05	.2	.120	3.917	.987	.038
.1	.4	.232	3.711	.984	.136
.15	.6	.331	3.505	.981	.260
.2	.8	.418	3.298	.976	.381
.25	1.0	.489	3.092	.971	.486
.3	1.2	.548	2.886	.964	.569
.35	1.4	.592	2.680	.956	.633
.4	1.6	.628	2.474	.946	.680
.45	1.8	.654	2.268	.934	.714
.5	2.0	.670	2.062	.919	.735
.625	2.5	.676	1.546	.863	.744
.75	3.0	.621	1.031	.768	.691
.875	3.5	.486	0.515	.593	.548
.95	3.8	.334	0.206	.395	.369
1.0	4.0	0	0	0	0

Table A4, Optimum Circulation Functions (2 Blades)

($\mu_0 = 5 \Rightarrow \lambda = .2 \Rightarrow J = .628$)

	Goldstein		Prandtl		
r/R	μ_o	G	f	F	G
0	0	0	5.099	.996	0
.04	.2	.124	4.900	.995	.038
.08	.4	.240	4.691	.994	.137
.12	.6	.344	4.487	.993	.263
.16	.8	.434	4.283	.991	.387
.20	1.0	.511	4.079	.989	.495
.24	1.2	.575	3.875	.987	.582
.28	1.4	.626	3.671	.984	.651
.32	1.6	.669	3.467	.980	.705
.36	1.8	.704	3.263	.976	.746
.4	2.0	.731	3.059	.970	.776
.5	2.5	.770	2.550	.950	.819
.6	3.0	.775	2.040	.917	.825
.7	3.5	.747	1.530	.861	.796
.8	4.0	.671	1.020	.765	.720
.9	4.5	.519	0.510	.590	.562
.96	4.8	.351	0.204	.393	.377
1.0	5.0	0	0	0	0

Table A5, Optimum Circulation Functions (2 Blades)

($\mu_0 = 8 \Rightarrow \lambda = .125 \Rightarrow J = .392$)

	Goldstein		Prandtl		
r/R	μ_o	G	f	F	G
0	0	0	8.062	.9998	0
.025	.2	.126	7.861	.99975	.038
.05	.4	.245	7.659	.9997	.138
.075	.6	.352	7.458	.99963	.265
.1	.8	.445	7.256	.99955	.390
.125	1.0	.525	7.054	.99945	.500
.15	1.2	.592	6.853	.9993	.590
.175	1.4	.649	6.651	.9992	.662
.2	1.6	.696	6.450	.9990	.718
.225	1.8	.736	6.248	.9988	.763
.25	2.0	.769	6.047	.9985	.799
.3125	2.5	.832	5.543	.9975	.860
.375	3.0	.873	5.039	.9959	.896
.4375	3.5	.899	4.535	.9932	.918
.5	4.0	.915	4.031	.9887	.931
.5625	4.5	.920	3.527	.9813	.935
.625	5.0	.918	3.023	.969	.932
.75	6.0	.874	2.016	.915	.890
.875	7.0	.728	1.008	.762	.747
.9375	7.5	.560	0.504	.587	.577
.975	7.8	.382	0.202	.391	.384
1.0	8.0	0	0	0	0

Table A6, Optimum Circulation Functions (4 Blades)

($\mu_0 = 5 \Rightarrow \lambda = .2 \Rightarrow J = .628$)

	Goldstein		Prandtl		
r/R	μ_o	G	f	F	G
0	0	0	10.198	.99998	0
.04	.2	.066	9.790	.99996	.038
.08	.4	.180	9.382	.99995	.138
.12	.6	.300	8.974	.99992	.265
.16	.8	.411	8.566	.99988	.390
.20	1.0	.506	8.158	.99982	.500
.24	1.2	.586	7.751	.99973	.590
.28	1.4	.652	7.343	.99959	.662
.32	1.6	.706	6.935	.99938	.719
.36	1.8	.750	6.527	.99907	.763
.4	2.0	.785	6.119	.9986	.799
.5	2.5	.848	5.099	.996	.859
.6	3.0	.881	4.079	.989	.890
.7	3.5	.887	3.059	.970	.897
.8	4.0	.851	2.040	.917	.863
.9	4.5	.714	1.020	.765	.729
.96	4.8	.505	0.408	.537	.515
1.0	5.0	0	0	0	0